Summer 7-25-2022

High-resolution Fiber Imaging for Pulsed Power Experiments

Karin Wikander Fulford
University of New Mexico - Main Campus

Karin Wikander Fulford

Candidate

Electrical and Computer Engineering

Department

This thesis is approved, and it is acceptable in quality and form for publication:

Approved by the Thesis Committee:

Mark Gilmore, Chairperson

Jane Lehr

David Yager-Elorriaga

HIGH-RESOLUTION FIBER IMAGING FOR PULSED POWER EXPERIMENTS

by

KARIN WIKANDER FULFORD

B.S., ELECTRICAL ENGINEERING
B.F.A., CERAMICS/SCULPTURE

THESIS

Submitted in Partial Fulfillment of the
Requirements for the Degree of

Master of Science
Electrical Engineering

The University of New Mexico
Albuquerque, New Mexico

July 2022

ACKNOWLEDGEMENTS

This project would not have been possible without the support and contributions of countless Sandia scientists, technicians, and peers. To them, I am sincerely grateful. I thank my advisor, Dr. Gilmore, and my mentor, Dr. Yager-Elorriaga for their generous patience, guidance, and teaching. I thank Dr. Patel for her teaching and visionary talent that inspired this work.

This work was funded by Sandia National Laboratories is a multi-mission laboratory managed and operated by National Technology and Engineering Solutions of Sandia, LLC, a wholly owned subsidiary of Honeywell International Inc., for the U.S. Department of Energy's National Nuclear Security Administration under contract DE-NA0003525, LDRD 226066.

This paper describes objective technical results and analysis. Any subjective views or opinions that might be expressed in the paper do not necessarily represent the views of the U.S. Department of Energy or the United States Government.

High-resolution Fiber Imaging for Pulsed Power Experiments

by

Karin Wikander Fulford

M.S., Electrical Engineering, University of New Mexico, 2022

B.S., Electrical Engineering, University of New Mexico, 2020

B.F.A., Sculpture and Ceramics, Kansas City Art Institute, 1998

Abstract

This thesis project explores the use of high-resolution plastic optical fibers for imaging emission from low-density plasmas in pulsed power experiments. These plasmas may be responsible for driving current loss and modifying the instability structure in magneto inertial fusion approaches such as Magnetized Liner Inertial Fusion (MagLIF); however, imaging their dynamics on the Z machine is an on-going effort. Addressing this, a compact and adaptable imaging system was developed to capture visible self-emission events in these extreme environments. Initiated as a tool for the Z machine, the project was named fiber imaging on Z (FIZ). The FIZ design utilizes a 2 mm diameter core commercial cable constructed of 13,000 individual acrylic fibers. The fibers are fused together to create a single high-resolution bundle. Different designs were investigated to cover a wide range of resolutions and field of views (3-700 microns and 0.05-45 mm, respectively), depending on the lens configuration. FIZ was fielded on Sandia's Z and Mykonos accelerators, as well as two other applications discussed within. Experiments have ranged from MagLIF on Z to hybrid x-pinches on Mykonos, with varying results. Extensive details of this investigation, including diagnostic development and application results, are presented.

TABLE OF CONTENTS

LIST OF FIGURES

LIST OF TABLES

CHAPTER 1: INTRODUCTION

1.1: Motivations

The principal motivation for this thesis project stems from on-going investigation of low-density plasmas on Sandia's large-scale current driven pulsed power accelerator, the Z machine. At a minimum, low-density plasmas are suspected to impact, 1) the performance of fuel filled target liner implosions for magnetized liner inertial fusion (MagLIF) experiments[1,2], and 2) reduce current delivery to an experimental load which is scrutinized through various power flow studies[3,4].

Details of the Z machine are provided in chapter 3, section 3.1, but key features include nominal 26 MA of electrical current delivered to a load target in about 100 ns[5]. In Z's vacuum center section, current is delivered to the target via a system of magnetically insulated transmission lines (MITLs). The MITLs are designed as wide short cone-shaped metal disks; several disks are stacked with alternating polarity and vacuum gaps between each disk (Figures 3.4 and 3.6). The vacuum gaps reduce down to about a few millimeters at the load target region. Current density is concentrated in the load region through post-hole convolutes that pass current from several MITLs down to a single pair of MITLs. This area (where the MITLs are reduced down through the convolutes) has about a 7.5 cm radius from the center target and is referred to as the inner MITLs region (Figures 3.6 and 3.7). From this process of gap reduction between the anode and cathode MITLs (often referred to as the AK gap), and current concentration to the load, plasmas are known to develop. These plasmas are noted about 70 ns into the pulse with densities in the order of 10^{14} cm^{-3} and temperature ranges from 100 eV on the surface to 100 keV in between the electrodes[3,4].

Early radiographic images of imploding, non-pre-magnetized MagLIF targets showed expected hydrodynamic plasma instabilities such as magneto-Rayleigh-Taylor (MRT)[6]. However, in 2013, images of the cylindrical liners revealed previously unobserved helical striations of high-density plasmas on the liner surface (Figure 1.1) when axially pre-magnetized[7]. Examination of these repeating helical structures led to a hypothesis regarding the magnitude of the axial magnetic field. For MagLIF shots, the magnitude of the pre-imposed axial magnetic field (B_z) is far weaker than the generated azimuthal magnetic field (B_θ) from the current driven implosion. Since MRT structures

tend to align themselves with the global magnetic field, this observation motivated a hypothesis that the axial magnetic field was flux compressed to magnitudes comparable to the azimuthal magnetic field. In this hypothesis, these plasmas are sourced from MITLs and magnetically driven towards the target region, where they flux compress the pre-imposed axial magnetic field to large values.

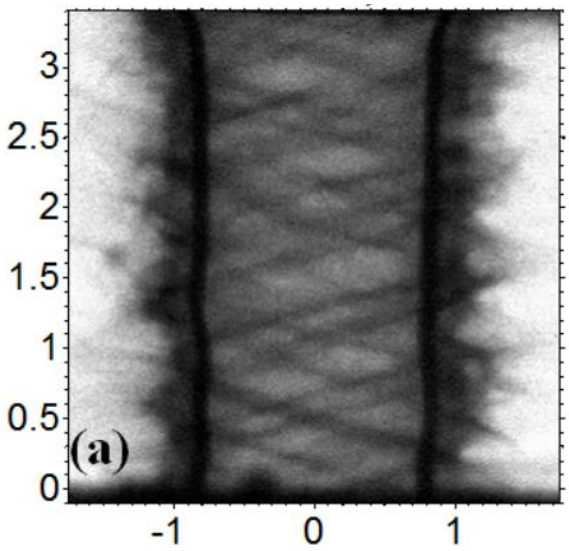

Figure 1.1 Adapted from radiographic image showing helical MRT structures in a MagLIF liner during implosion[7].

In general, imaging plasma dynamics is a widely used and valuable method to help witness the origin, density gradients, and flow patterns. At Z current optical approaches include instruments such as streak cameras, multi or single frame gated cameras, and avalanche photodiodes. However, to capture low-density plasma, higher resolution is needed. As well, optical devices that are coupled to single fibers lack full intensity spatial information and other imaging systems require time-consuming alignment and can image only one location. An example of this is the Self Emission Gated Optical Imager (SEGOI)[8]. This system utilizes a pre-existing image path going to cameras located outside of the Z highbay. As shown in Figure 1.2, a large lens (focal length = 400 mm) is placed within line of sight (green line in the Figure) to the target but outside the blast shield. The lens is track aligned with a periscope which passes the image along a 50 m optical relay system. The

image going to the gated cameras is limited to wavelengths between 540-600 nm and spatial resolution is ~50 microns. As well, this system takes some time to install and align; therefore, increasing options for optical imaging diagnostics for Z is an ongoing effort but designs demand careful consideration.

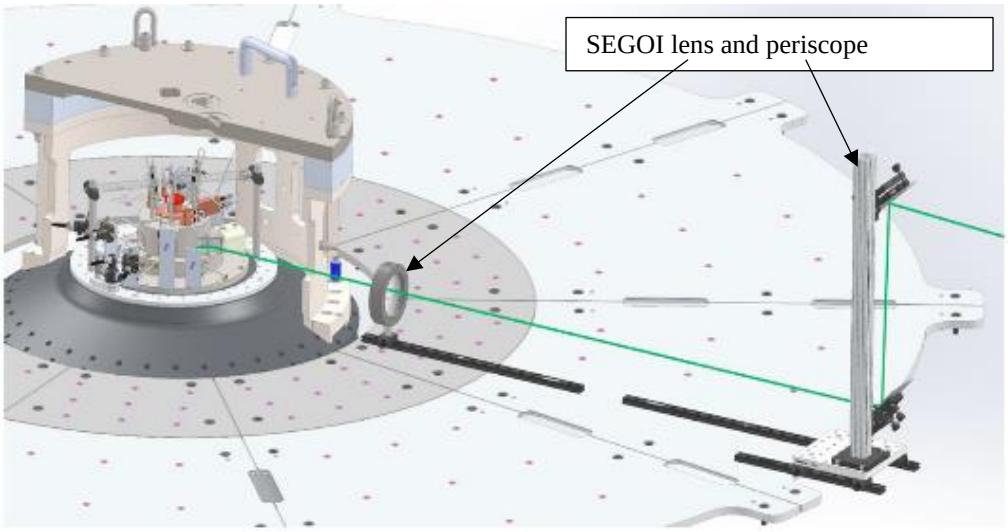

Figure 1.2 Adapted image of SEGOI imaging system inside Z center section[8]. The green line displays the optical axis and alignment path needed for operation. This is an example of one current imaging diagnostic that requires significant time to install and align (~1hour).

The pulsed power environment at Z is complex with environmental, structural, and programmatic obstacles. Diagnostic designs must consider the lack of optical ports, electromagnetic inference, mechanical shock, and a strict shot schedule. Furthermore, unpredictable light intensities and nanosecond timing are inherent challenges to documenting self-emission and instability formations. These complexities provide the problematic backdrop for imaging self-emission on Z, and define the concerns addressed in this work. Hence, it was the goal of this project to explore a new method of imaging attending to these challenges.

Given the challenges at Z and additional space limitations at the load and inner MITL region, fiber imaging was suggested as an imaging technique to explore. Fiber imaging is well established for medical applications and manufacturing advancements in plastic optical fiber (POF) have brought to fruition an interesting high-resolution product.

Some benefits to fiber imaging include versatile design options, inexpensive materials, and micron spatial resolution. The specifics of a commercial high-resolution POF are discussed in chapter 2, section 2.2, as it was the key component for this project. With that said, we next introduce an overview of this work.

The scope of this thesis project was to design, develop, and field test a high-resolution fiber based diagnostic instrument for imaging in the visible range. As designed for Z, the name of the diagnostic is fiber imaging on Z (FIZ). A basic diagram of the design is provided in chapter 2, Figure 2.1. With lens configurations at either end of the fiber, different resolutions and field of view results can be achieved as summarized in Table 2.1. As well, bench testing proved the capability for imaging self-emission events.

During the course of this project, application ideas expanded, and a summary of applications is provided in chapter 3, Table 3.1. In short, while imaging low-density plasmas was a goal for some MagLIF shots on Z, imaging damaging shrapnel was also proposed and fielded. Unfortunately, due to camera complications, no images were captured during any of the Z shots; however, high quality pre-shot images showed the potential of this diagnostic. Self-emission images were successfully recorded on the Mykonos accelerator during hybrid x-pinch studies (see section 3.2). For this application the goal was to observe the time evolution of plasma instabilities as the X-pinch underwent radiative collapse. Other successful trials at Mykonos included inserting the imaging fiber along the pre-existing laser shadowgraphy path (section 3.2.2). Here the goal was to test fiber transmission of initially coherent 532 nm light, and also observe plasmas through density gradients. The encouraging results from this test have led to the planning of similar methods on Z using the imaging fiber and a laser backlighter. The last application presented is video recording of mechanical motion in vacuum. The objects of interest are MagLIF coils that undergo pulsed power testing prior to their deployment on Z. The motion is due to magnetic pressures during the pulse and observations of this motion will assist with coil development.

This thesis provides extensive information regarding the process and details of the project including unplanned development activities and the above-mentioned application expansions. Literature searches for pulsed power platforms utilizing high-resolution POF

imaging did not expose previously published work; therefore, the diagnostic presented here is possibly a novel method for such environments.

This work was performed at, and funded by, Sandia National Laboratories in Albuquerque, New Mexico. Sandia National Laboratories is a multi-mission laboratory managed and operated by National Technology and Engineering Solutions of Sandia, LLC, a wholly owned subsidiary of Honeywell International Inc., for the U.S. Department of Energy's National Nuclear Security Administration under contract DE-NA0003525, LDRD 226066.

This paper describes objective technical results and analysis. Any subjective views or opinions that might be expressed in the paper do not necessarily represent the views of the U.S. Department of Energy or the United States Government.

1.2: Background

For over a century, scientists have toiled to understand the fundamental physics contained within nuclear interactions. Astrophysics, national defense, and commercial nuclear power all have been motivating fields to propel this research. Starting with the stars, physicists in the early 1900's postulated a nuclear source for cosmic illumination and proposed that changing atomic mass produced the visible emission[9]. Following these astronomical theories, nuclear research was galvanized by the events of WW II which ushered the capability of nuclear fusion (and fission) on earth. The demonstration of immense power was quickly transformed into a commercial source for electrical power. By 1970, over twenty fission reactor power plants were in operation in the United States[10]. The combination of these three motivators inspired the invention of particle accelerators, culminating years later to the world's largest pulsed power facility.

The Z machine pulsed power accelerator at Sandia National Laboratories represents decades of discovery and innovation in nuclear research. The road to pulsed power for Sandia began during the 1960's with continued weapons research at the Atomic Weapons Research Establishment and Physics International[11]. The appeal to produce radiographic imaging of explosive events led to the development of a high-voltage vacuum diode and Marx generator which Sandia promptly adopted. These advancements instigated a series of large-scale pulsed power radiation experiments at Sandia which, by the mid-70's,

solidified development of pulsed power facilities for inertial confinement fusion (ICF) research[12].

In 1996 Sandia's Particle Beam Fusion Accelerator II (PBFA-II)[13] was converted to optimize and scale the new wire array z-pinch radiation source, demonstrated earlier on Sandia's Saturn accelerator[14]. The reconfigured PBFA accelerator was named the Z machine, producing about 1.6 MJ of soft x-ray energy. Due to experimental successes and increasing demand for Z shots, the machine was refurbished from 2003-2007. This was termed the ZR project to improve reproducible high-current experiments and fortify the machine for daily operations[15].

After ZR, the improved Z machine, now fully outfitted with a high-power laser backlighter (Z-Beamlet in 2001)[16] among the ZR advancements, could support a host of research topics including material studies, the weapons program, and ICF. At this point Z was firmly established as the world's most powerful current driven accelerator delivering 26 MA to a target within ~100 nanoseconds. X-ray production increased to 2.7 MJ and daily shots became the norm[5].

By this time magnetized target fusion (MTF)[17] was also suggested as a method to compress a capsule to fusion conditions. Both ICF and MTF techniques have advantages and disadvantages. In order to capitalize on the advantages, simulations utilizing and optimizing both approaches were performed. In 2010, results of these simulations revealed promising fusion yields by introducing a pre-applied magnetic field and laser pre-heating of the fuel[18]. The combination of concepts became known as MagLIF (magnetized liner inertial fusion) and has since flourished into a primary model for fusion studies at Z.

Parallel to the ICF/MagLIF work, Sandia also continued to advance pulsed power methods and plans for future facilities. Collaboration with academia (Institute of High Current Electronics at the Russian Academy of Science, and University of Michigan), and industry (International Technologies for High Pulsed Power, France) led to the development of linear transformer drivers (LTD)[19,20] and the construction of Mykonos. Mykonos is a 1 MA, 100 kV pulsed power accelerator with modular voltage adding capability and interchangeable vacuum chambers[21]. It is housed within the Z facility complex and is often used to assess new diagnostic concepts and techniques for the Z machine.

Today, both Z and Mykonos are in constant operation and continue to support astronomical, national defense, and nuclear power research. The Z machine fields a variety of experimental target configurations and is primarily is used for ICF, dynamic materials properties (DMP), high energy density (HED), and x-ray radiation research. While Mykonos, being a smaller machine with reduced diagnostic capability, remains a testbed for focused small-scale studies. Concepts such as electrothermal instabilities, novel x-ray sources, spectroscopic configurations, and imaging techniques, represent a limited sample of the studies performed at Mykonos. More details of the Z machine and Mykonos are discussed in later sections as they were platforms utilized during this project.

1.3: Document Organization

The next three sections of this document are organized as follows. Design and development, including bench testing and characterization, are presented in Chapter 2. Here we will introduce the basic diagnostic design and review details of the supplies and equipment utilized for testing. Discussion of lateral investigations such as fiber preparation and environmental EMP testing will also be provided.

Applications and results are covered in Chapter 3. This will include specific configurations for the diagnostic and communications on the Z machine and Mykonos accelerators. Outcomes from these shots will be presented and discussed. As well, completion and current plans for complementary applications are provided.

Chapter 4 will conclude with a summary of work, application successes and failures, and ideas for further developments will be shared.

CHAPTER 2: DIAGNOSTIC DESIGN AND DEVELOPMENT

2.1: Basic Design

Addressing the environmental, structural, and programmatic obstacles described above, we present a compact and adaptable imaging system as a technique to capture self-emission events during pulsed power experiments. The concept was initiated as a tool for the Z machine; subsequently three primary goals guided the design: versatility, fast and

easy installation, and multi-viewing capability. The project was named Fiber Imaging on Z (FIZ) and the design utilizes an inexpensive commercial high-resolution plastic optical fiber (POF) coupled between two air gapped lens configurations. A focusing lens forms an image onto the face of the transmitting POF. At the receiving end, a magnifying lens projects the transmission onto a gated sensor. Figure 2.1 illustrates the basic design and operation of the system.

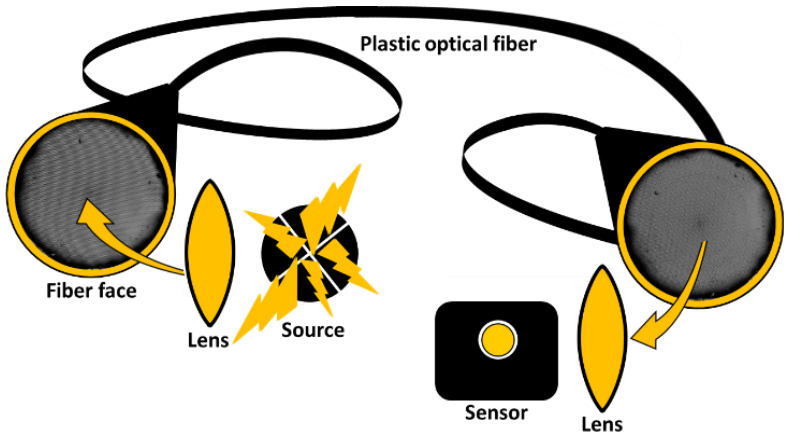

Figure 2.1 Diagram of basic imaging system using a high-resolution plastic optical fiber (POF) to transmit an image. An image is created on the face of the fiber and transmitted over many meters to a camera sensor. Air (or vacuum) gapped lens configurations coupled at each end of the fiber control magnification and focus onto, or out from, the fiber face.

2.2: Component Specifications

2.2.1: High-resolution plastic optical fiber

At the heart of this instrument is a specialty fiber optic cable which is commercially available and relatively inexpensive, making it an ever more appealing product. The manufacturer is a company in Japan, Asahi Kasei Corporation, and the fiber (part number: MCL-2000-24) is constructed of 13,000 individual fiber cores[22]. Figure 2.2 shows the connectorized 2 mm fiber face and a detail of the multi-core structure. The core material is polymethyl methacrylate (PMMA) and the jacket material is polyethylene (PE). Each individual fiber has an approximate 15 micron diameter. The sum of the fused cores creates a 2 mm diameter fiber face; 2.4 mm diameter with jacketing. Based on the approximate

index of refraction for PMMA (1.49)[23] the fiber's phase velocity was calculated to be 0.20 m/ns. The fiber is step-index multimode with a numerical aperture of 0.5[22]. Due to the large diameter, SMA connectors are commonly used. Attenuation is estimated to be ~0.1 dB/m for 450-600 nm wavelengths[24]. For a 20 m length fiber, that works out to be about 40% attenuation for the visible range. The attenuation is notably higher for wavelengths outside this range. However, while typically perceived as a drawback, high attenuation can be an advantage for viewing bright self-emission.

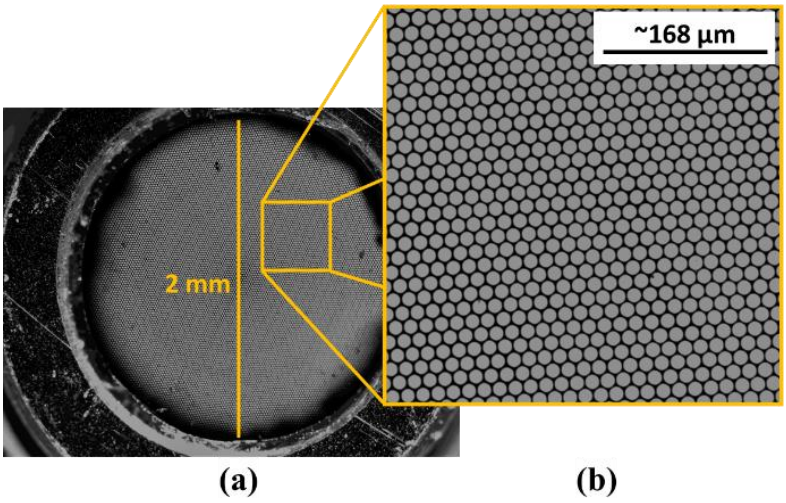

Figure 2.2 (a) Photograph of 2 mm POF fiber face secured in a (SMA) ferrule. (b) Enlarged cross section of PMMA POF (MCL-2000-24) highlights the individual fibers, each ~15 µm in diameter.

As Polishuk points out, there are several advantages and disadvantages when using POF[24]. One big advantage is durability compared to silica fibers. While acrylic has the potential to fracture, it is far more flexible and resilient to bending and shock, especially for long runs. POF is light weight, transmits in the visible range, and is unaffected by electromagnetic interference. Also, POF is relatively inexpensive, making it a reasonable consumable for explosive pulsed power environments. The main disadvantage is attenuation. PMMA has high transmission loss compared to silica and has the potential to become brittle and reduce transmission with prolonged UV exposure[25,26].

2.2.2: Fast cameras

For this project, primary and secondary cameras were used. The primary camera was a Princeton Instruments intensified charge coupled device (ICCD, PI Max 4, 1024f)[27]. This model has a C mount lens port, a 0.48 ns minimum gate, and a 13.3 x 13.3 mm sensor with 13 μm pixel size. Pixel ratio of imaging fiber to this sensor is 1.15. In general, gate times varied but gain was 1x most of the time. Internal cooling helps reduce the noise floor, but this capability is limited in confined spaces.

An ICCD is a CCD with an added intensifier. CCD technology has been around for several decades and is widely used in scientific fields as well as in medical and office equipment. High light sensitivity, nanosecond exposures, and high-quality imaging are some beneficial features of CCD cameras[28]. As described by Princeton Instruments, a CCD uses a silicon sensor that inputs photons and outputs electrons in a 1:1 ratio[29]. Sensors are constructed with different materials depending on the wavelength or bandwidth to be viewed. Layers within the sensor start with the input of photons through a micro lens and polymer. A PN junction is then employed to output electrons. The electrons are stored in an array of pixel wells creating voltage that is translated to a digital signal through an analogue to digital converter (ADC); the digital signal is then displayed on a monitor.

Adding an intensifier to the CCD increases the number of electrons sent to the pixel array. The intensifier has three main components: photocathode, microchannel plate (MCP), and phosphor screen[30]. The photocathode converts photons to electrons and the MCP provides electron multiplication. Electrons are accelerated through biased layers leading them to interact with the phosphor layer which converts them back to photons and transmits via fiber optic to the CCD array. Furthermore, electron production is related to the camera gain by changing the number of electrons used to create the digital signal. As gain is increased, the multiplication factor of electrons also increases for the digital display, therefore increasing the sensitivity for low-light or fast gate imaging. Theoretically, this is a linear process, but our cursory measurements shown in Figure 2.3 demonstrate non-liner intensity increase with increasing gain.

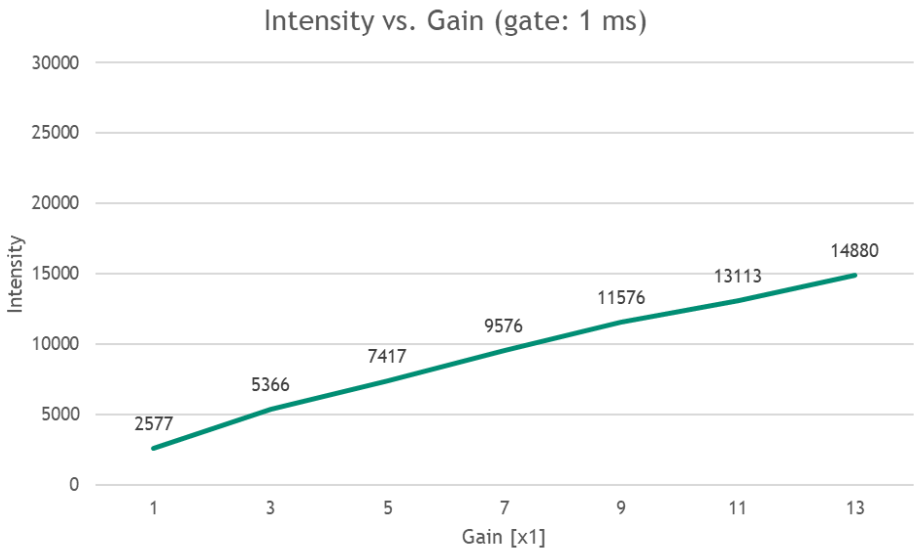

Figure 2.3 Measurements indicate a non-linear process of intensity vs. gain for a PI Max 4 ICCD camera.

The second camera used for this project was a Phantom® VEO 1310, complementary metal oxide semiconductor (CMOS), instrument[31]. This camera has a minimum gate of 1 microsecond and maximum 10,860 frames per second at the highest resolution. The pixel size is 18 µm with 1.2-megapixel sensor resolution. The pixel ratio of imaging fiber to this sensor is 0.83. While the gate of this camera is slower than the PI Max, it is more robust against high intensity light and electromagnetic interference. CMOS sensors are essentially an array of transistors and photodiodes, each putting out a voltage signal corresponding to a pixel position[32]. For the purposes of this project, the VEO was not used for self-emission, or system characterization, but rather for slower pulsed power events such as structural movement discussed in sections 3.1.3 and 3.3.

2.2.3: Sources

For system characterization, two input sources were used at the test bench. 1) an LED backlit United States Air Force (USAF) 1951 resolution target (glass window, two sizes)[33,34] and 2) a known emission xenon arc lamp[35,36,37]. An example of the bench setup, using the resolution target (backlit with a flashlight), is provided in Figure 2.4. The size

and spacing of the black line patterns are defined by established MIL-STD-150A standards[38]. Group and element values are noted in Figure 2.5. Subjective (by eye) resolution can be determined using available charts or Eq. 1. Depending on the preferred units for resolution, line pairs per millimeter can be converted to microns via the process outline in Eqs. 1-3. Utilization of this target allowed for characterization of different focusing lenses positioned at the source end of the imaging system. Results are reviewed in section 2.3.

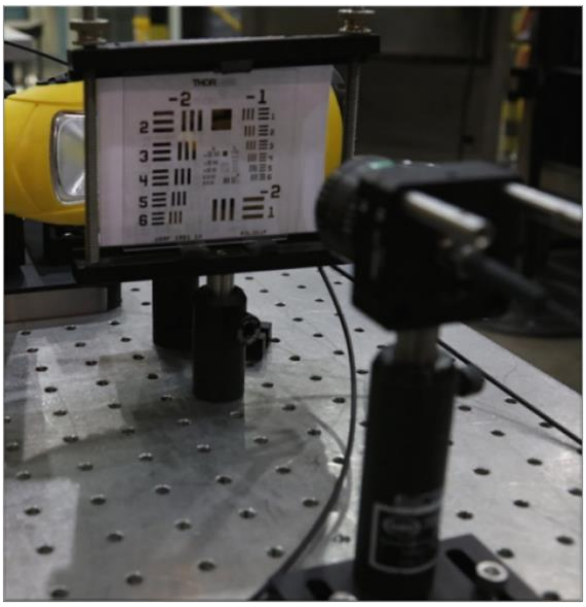

Figure 2.4 Bench setup of glass window USAF resolution target with flashlight backlighter and white paper diffuser.

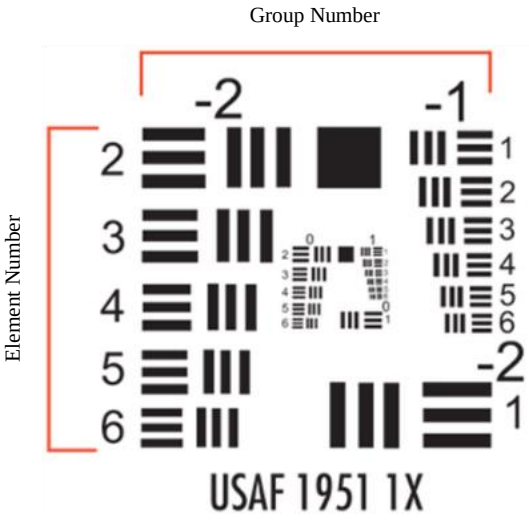

Figure 2.5 Display of defined group numbers and element numbers used to find (lp/mm) resolution in Eq. 1.

(Eq. 1) $$\frac{line\ pair}{millimeter} = 2^{\left[Group\ Number + \frac{Element\ Number - 1}{6}\right]} \left(\frac{line\ pair}{millimeter}\right)$$

(Eq. 2) $$\frac{microns}{line\ pair} = \frac{1000\left(\frac{microns}{millimeter}\right)}{Eq.1\left(\frac{line\ pair}{millimeter}\right)}$$

(Eq. 3) $$\frac{microns}{one\ line} = \frac{Eq.2}{2}\left(\frac{microns}{one\ line}\right)$$

Also, from the USAF resolution target, field of view (FOV) can be estimated. An example of this process is demonstrated using the image, lineouts, and calculations provided in Figure 2.6. (Note, Figure 2.6a and Figure 2.6b are provided on the next two pages.) By analyzing the image in MATLAB®, a region of interest (ROI) can be defined (Figure 2.6a). Taking the average of the ROIs, and plotting with a curve fit, the pixel edge values of the black lines can be estimated. This was done for two different ROIs (within the same target element) to get an average line width measurement. Taking that average and given the known micron width of the corresponding USAF black line leads to a conversion factor, micron/pixel. The height of the image in pixels can also be measured in MATLAB® (Figure 2.6b). Multiplying the measured height in pixels with the conversion factor determines a spatial field of view in microns.

Field of View Calculation Using USAF µm Resolution

- Resolution of 4-1 element = 31.25 µm per Eqs. 1-3
- Average width of ROIs = 31.5 pixels
- Conversion factor = 0.99 µm/pixel
- FOV for this image: 0.99*310 = 306.9 µm

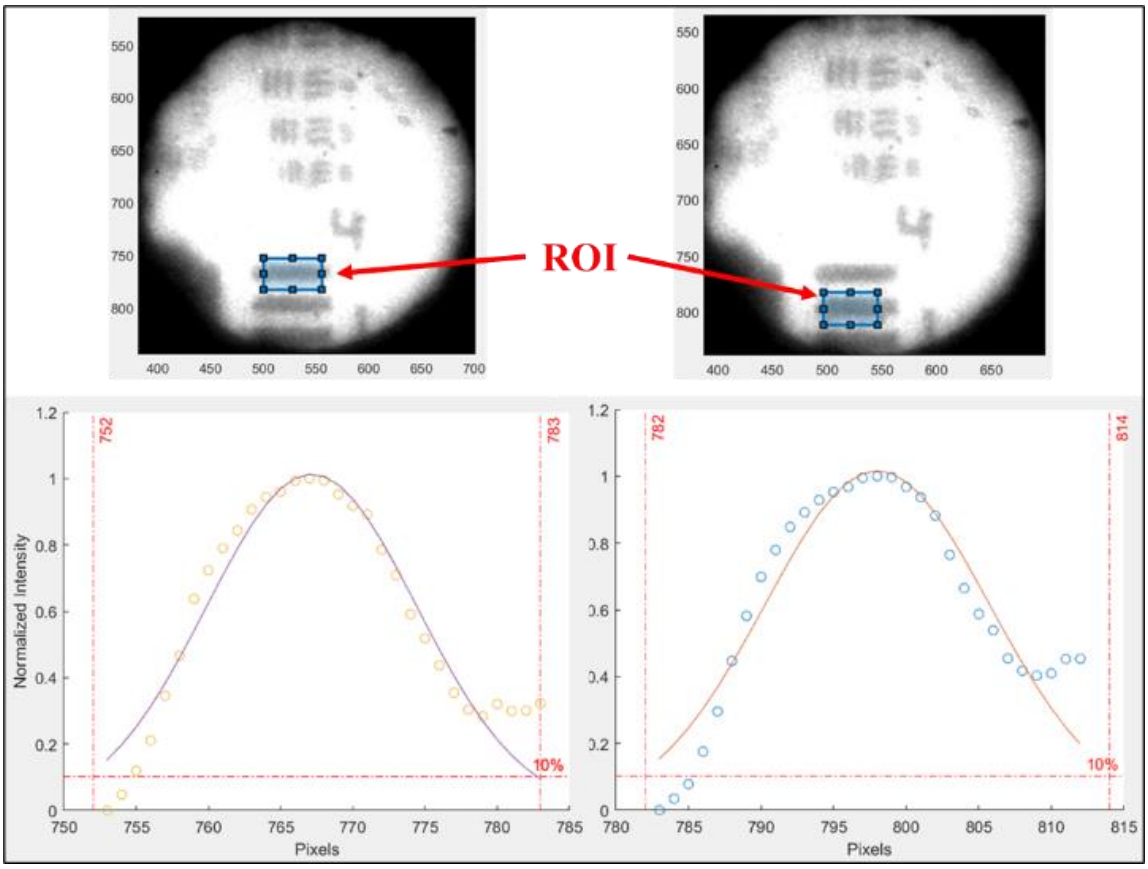

(a)

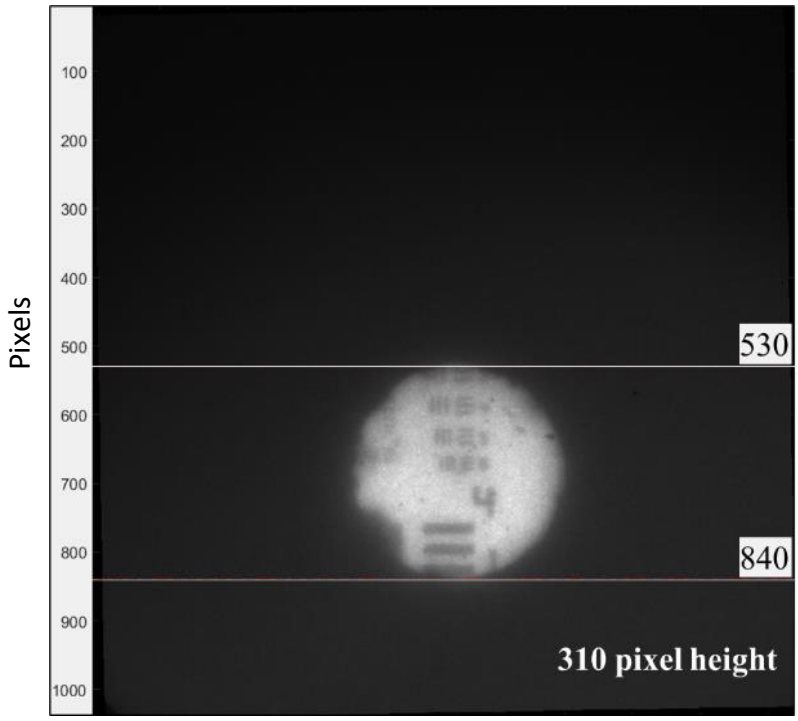

(b)

Figure 2.6 Field of view calculation using the USAF resolution and MATLAB® to construct a conversion factor for a given image. The known micron resolution of the 4-1 line and the average of ROIs in (a) create the conversion factor for this image. The image height in pixels is determined in MATLAB® (b) and the conversion factor is applied to find the FOV of the supplied image.

To determine the capability for self-emission imaging, an open access Oriel arc lamp (60000 Q series)[35] with a Xenon flash bulb (model 6427)[36] was pulsed with 800 mJ of energy (model 68826)[37]. This flash bulb is constructed with two electrodes, an anode and cathode. There is a 3 m gap between the electrodes. The vacuum sealed glass envelope is filled with Xenon gas and when high enough voltage is applied to the electrodes, the gas is ionized forming a short-lived plasma. This flash bulb is broad in the visible range and has a reliable FWHM arc of ~9 μs. This source is well characterized and broad in the visible range[36]. The PI Max camera and lamp were triggered from a delay generator (DG), and timing of the signals were monitored with an oscilloscope. A fiber-coupled photodiode transmitted the arc emission to the scope as shown in Figure 2.7.

Using the camera software (LightField®,[39]), the camera trigger and gate were adjusted to capture plasma growth at different times through the arc. Gate was

progressively reduced when imaging toward the peak of the bright emission. Images from this configuration are provided in section 2.3.

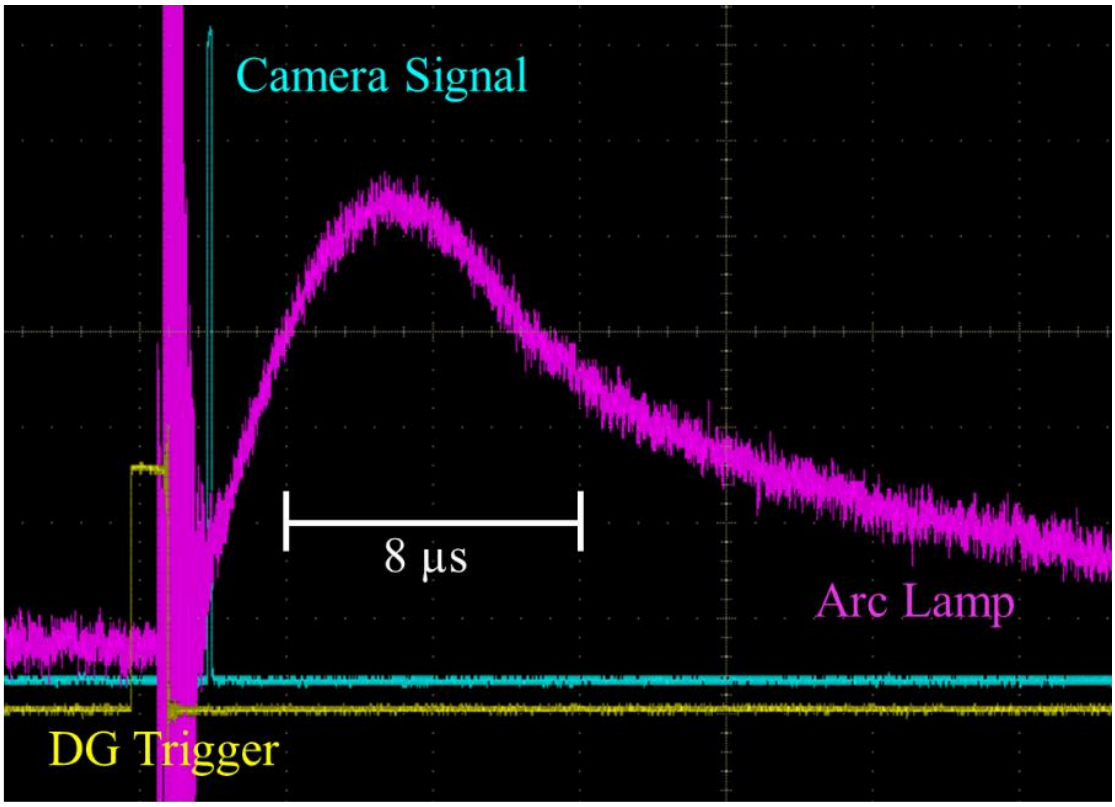

Figure 2.7 Oscilloscope screen shot showing the DG trigger and subsequent camera and lamp signals. The lamp signal was transmitted via silica fiber optic to a photodiode.

2.2.4: Lenses

On the source side of the system, three different lenses were explored. They included a small diameter aspheric lens (<10 mm)[40], a wide-angle lens (67° diagonal field of view)[41] and a microscope objective lens (20x)[42]; all with different focal lengths (fl). These lenses were chosen to verify the adaptability of the system and confirm the tradeoffs. In particular, the objective lens can offer a few microns resolution (section 2.3), but most objectives also have few millimeters working distance, which is not practical for targets on Z. The small aspheric can fit into space-limited hardware configurations with limitations on resolution and field of view (FOV). Also, the wide-angle, offering a large FOV, is a camera lens designed to couple to a large sensor, therefore much of the image is lost and

not well coupled to a 2 mm fiber face. Despite this deficiency, the wide-angle was used to capture x-pinch self-emission images on Mykonos (section 3.2); therefore, validating the success and usefulness of the tool even though the imaging is not yet optimized.

On the output side of the system, the imaging fiber was coupled to the camera sensor through a Thorlabs matched achromatic doublet pair. A 2x (model MAP1050100-A, fl = 50 mm input; fl = 100 mm output)[43] was primarily used for characterization, while a 3x (model MAP1030100-A, fl = 30 mm input; fl = 100 mm output)[44] was used for the applications discussed in chapter 3.

2.3: Bench Testing

As previously indicated, the test bench setup included an input source, either the backlit resolution target or the Oriel arc lamp, coupled to the imaging fiber through one of the three lenses discussed. For bench testing, the length of the imaging fiber was 20 meters with commercial polishing on each fiber face. The output image from the fiber was coupled to the camera sensor through magnifying lens configuration. For the three input lenses tested, a summary of lens properties, test conditions and subjective resolution results is supplied in Table 2.1. Figure 2.8 highlights image results from the three lens types. A full sensor example (Figure 2.8a) is provided to illustrate the magnified output (2x) relative to the sensor. In Figure 2.8b a 20x objective was positioned about 2 mm from the USAF target[33] and produced the smallest resolution achieved with this system, ~3 μm. Results from the small aspheric (Figure 2.8c) indicate an estimated 7.8 μm resolution, and the wide-angle (Figure 2.8d), ~630 μm.

Table 2.1: Summary of Input Lens Testing

Lens Type	Objective	Aspheric	Wide-angle
Part Number	Swift 20x 0.4	C220TMD-A	M0814-MP2
Specification	20x	7.2 mm OD	DFOV 67.1°
Focal Length (mm)	2	11	8
Numerical Aperture	0.40	0.25	n/a
USAF 1951 Group-Element Number	7-3	6-1	(-1)-5
USAF 1951 Resolution	3.1 µm 161.3 lp/mm	7.81 µm 64 lp/mm	629.96 µm 0.794 lp/mm
Field of View (approx. mm)	0.05	0.3	45
Target to Lens (approx. mm)	2	10	195
Lens to Fiber (approx. mm)	88	33	19

Table 2.1 Summary of properties and test results for three different input lenses. Corresponding images are provided in Figure 2.8.

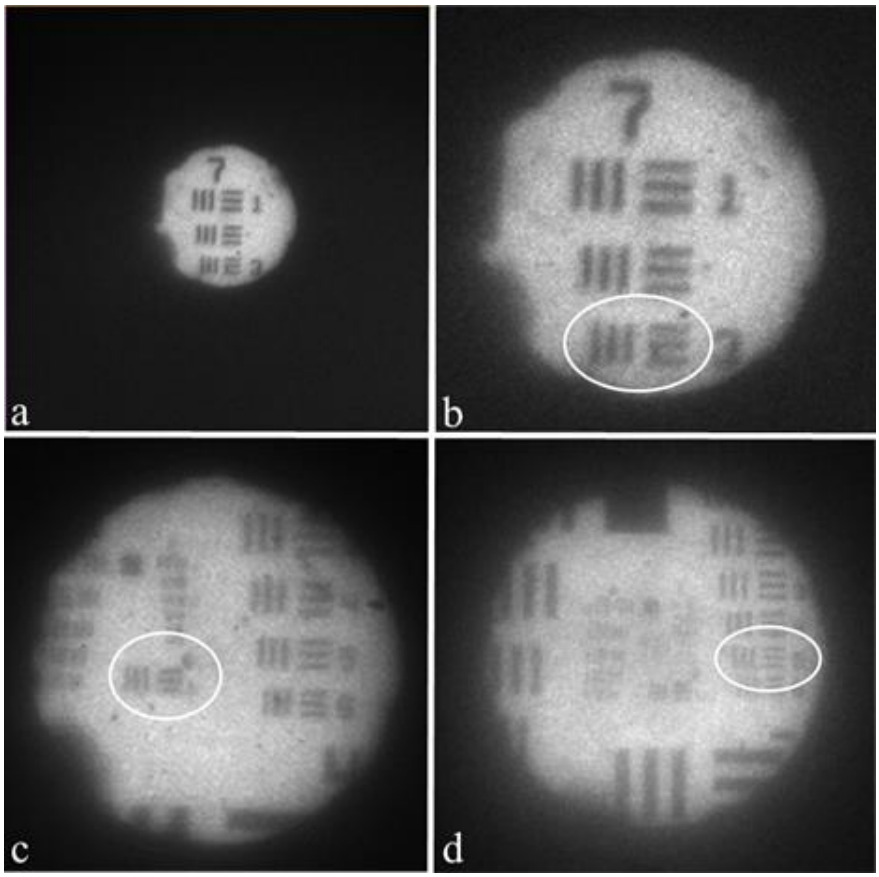

Figure 2.8 One full sensor example of the PI Max 4, and three cropped images indicating the resolvable USAF target lines used to quantify the resolutions of the three lenses listed in Table 2.1. All configurations here used the same output lens, a 1:2 matched achromatic doublet pair. (a) The 2 mm diameter fiber face is magnified onto a 13.3 x 13.3 mm ICCD sensor with 13 µm pixel size. Pixel ratio of fiber to sensor is 1.15. (b) 20x objective lens, 7-3 circled. (c) Aspheric lens, 6-1 circled. (d) Wide-angle lens, (-1)-5 circled.

Imaging the emission of the arc lamp was primarily accomplished through utilization of a delay generator (DG). Three channels of the DG sent trigger signals to the oscilloscope, lamp, and camera. There were negligible delays between each signal. Delay control of the camera trigger was modified through the camera software. Using the small aspheric lens, with fl = 11 mm, a reference image of the lamp electrodes was taken. External lighting was needed to illuminate the electrodes as shown in Figures 2.9 and 2.10. This reference image provides the FOV and focus for the self-emission imaging to follow in Figure 2.11. These fast-gate images provided the proof-of-concept needed to move forward with application planning and implementation discussed in the next chapter.

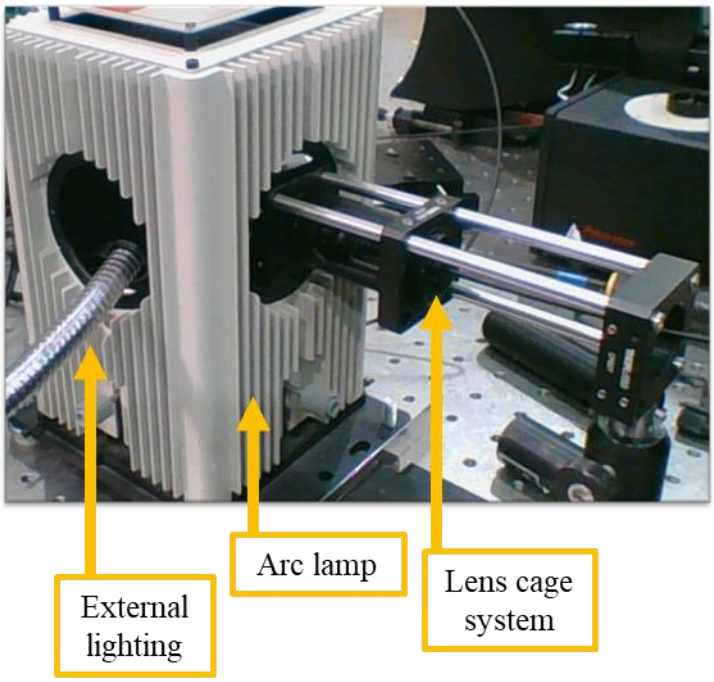

Figure 2.9 Bench configuration to image lamp electrodes. This provides reference for the field of view and focus during self-emission imaging.

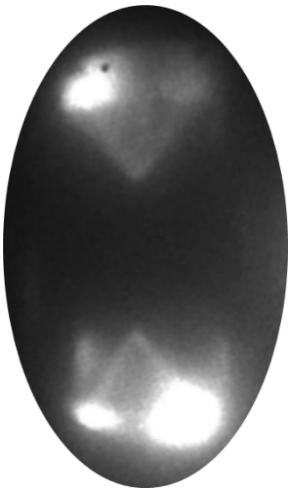

Figure 2.10 Fiber image of the arc lamp electrodes using aspheric lens with fl = 11 mm. Given 3 mm gap, FOV is estimated to be 6 mm.

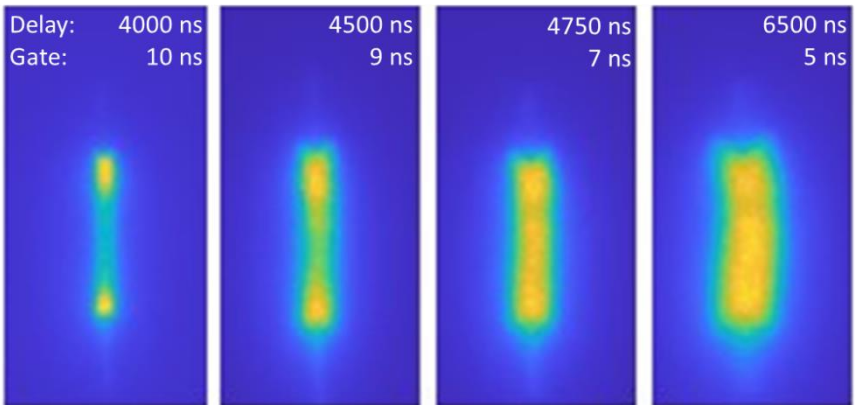

Figure 2.11 Fiber imaging of self-emission at different stages along the lamp arc. Delay is relative to camera triggering. Approximate arc peak is 9400 ns. See Figure 2.10 for FOV and focus reference.

2.4: Complementary Developments

During the course of this project several questions and situations arose that warranted tangential exploration. Of immediate importance was the question of ICCD camera functionality in a high radiation environment. Specifically, we needed to know if electromagnetic interference (EMI) would prevent successful imaging and how EMI would affect the noise floor of the image. This prompted a series of tests to ensure data capture during planned Z shots. Results from this testing are provided in the next section.

Additionally, as this diagnostic depends on the quality of the POF, it was a natural extension to investigate in-house preparation, i.e., cutting, terminating, and polishing. This led to some interesting discoveries and increased capability to work with this fiber.

2.4.1: EMI testing

In preparation for future experiments at Z, EMI testing was performed with the ICCD PI Max camera. The camera was placed inside a screen room in the Z highbay. The camera was triggered by the central control system and an ethernet communication line was established to monitor camera operations. Testing during four Z shots (each with different loads) first reveled interruption in the data transfer. The camera was triggering with an accurate gate signal, as recorded by the central system, but the data image did not reach the laptop. As well, this camera does not have internal memory so no data could be retrieved. Our remedy was to try adding a screen box, inside the screen room, and place lead plates around the box to help shield x-rays as shown in Figure 2.12. This fix was successful as data was received for the next three shots and we proceeded to investigate changes to noise floor.

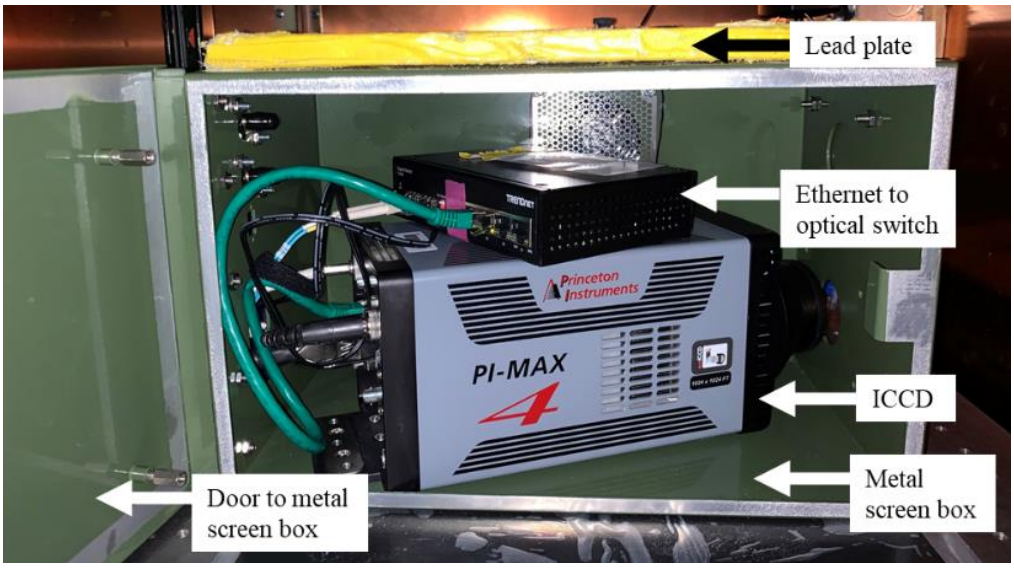

Figure 2.12 Configuration for EMI testing within the Z highbay. The ICCD camera and ethernet switch was placed inside a metal box with lead shielding placed around the box.

In general, the noise floor of the PI Max ICCD is about 600 counts. Putting the camera in a box, with the door closed, did reduce air flow for internal camera cooling. Consequently, the camera struggled to maintain the temperature setpoint (20°C). A computer fan was added on the outside of the box to help draw out heat, but this provided minimal impact. It is generally understood that camera temperature can contribute or affect the noise floor, but specific quantification requires further examination.

Essentially, our findings showed that the background noise did increase by about 200-300 counts with occasional pixel blooming[45]. (For this camera, pixel saturation is approximately 65,000 counts so blooming is typical when a pixel electron well is reaching this maximum.) The camera gain was 1x and gate was 0.48 ns for all of these shots. During an 85 kV Z shot, average noise floor increased by about 40% and increased about another 6% for a 90 kV shot. Recovery of the sensor after the shot was verified, i.e., noise floor was the same before and after the shot. A summary of the three data-collecting EMI test results is provided in Table 2.2.

Table 2.2: Summary of EMI Testing

Shot Date	1/24/22	1/26/22	1/27/22
Shot voltage (kV)	85	85	90
Camera setup	box only	box with fan and shields	box with fan and shields
Mean count	826.637	844.116	876.562
Std. deviation	394.374	378.358	404.407
Highest count value	7616	52027 (blooming)	7921
Percent increase from base noise floor (~600 counts)	37.77%	40.69%	46.09%

Table 2.2 Summary of results from EMI testing of the ICCD PI Max camera during four Z shots and located at the Z highbay.

2.4.2: Fiber preparation

In-house POF preparation (i.e., cutting, terminating, and polishing) was an organic tangent to this project which yielded increased knowledge and technical capability. A noteworthy lesson included the compatibility of CO_2 lasers with acrylic. As described by Anderson *et al.* [46], it is possible to cut and polish simultaneously using a laser. However, for high-resolution imaging fiber, it was unknown if this process would impact fiber pixel performance. Preliminary results from our testing of this process were encouraging. Cutting multiple fibers at once, with a relatively polished surface was achieved but an optimized approach is not yet determined. It appears that a higher watt laser (e.g., 150 W compared to a 40 W, Figure 2.13) with a fast feed rate may ultimately provide a better fiber face for this imaging fiber, but more work is needed to confirm.

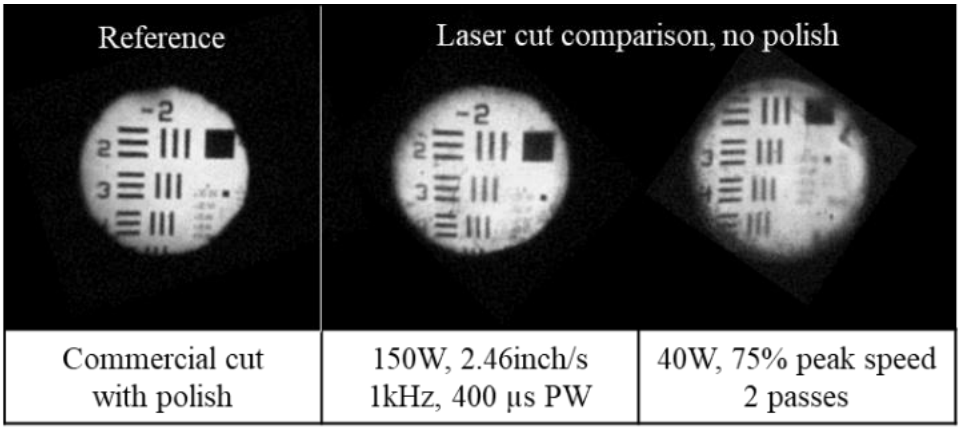

Figure 2.13 Comparison of in-house laser cut fiber with reference commercial cut. Results indicate fast high-power laser could lead to optimal simultaneous cutting and polishing. Further investigation is needed.

In addition to the laser cutting, other cutting methods were utilized such as cleaving with a guided straight razor, snipping with wire cutters, and scoring through with a hot knife. While laser cutting is defiantly the most efficient for cutting many fibers at once, the hot knife approach was found to have the best results when preparing a single fiber.

Before the end of the fiber can be polished, it needs to be stripped and glued into a ferrule or something similar. Two-part epoxy or super glue were successfully used for this task. It took many trials to optimize the location of the glue and the amount of glue to use. (With SMA connectors it was easy to accidentally glue the nut which will prevent connecting the fiber to an optical component.) Along with gluing, a hexagonal crimping tool was used to further fasten the backend of the ferrule to the jacketed portion of the fiber.

Learning to polish this fiber was another trial-and-error process that required time to refine. The POF used for this project has a relatively large diameter face and is, in general, softer than silica; therefore, it scratches more easily and requires tedious cleaning and water flushing to achieve an optimal polish. Both manual and machine polishing methods were utilized for this work, and both methods require a fair amount of setup and time to work from course to finer grit. Like laser cutting, machine polishing is preferred when more than one fiber is needed. If just one fiber, then manual polish is simplest but laborious. Both methods use a series of papers, progressing to finer grit, and frequent water

flushing is always required. An example of multi-fiber machine polishing is shown in Figure 2.14. The fiber plate shown holds up to 9 fibers with SMA connectors. Even with this automated approach, results may vary.

Figure 2.14 Multi-fiber polishing plate on a Domaille Engineering, LLC, advanced polishing machine, model HDC-5100. Nine fibers are SMA connected and automatically polished using progressively finer polishing pads.

Additionally, a simple custom inspection instrument was designed by a team member to evaluate polishing results. Using standard optical components, the tool is essentially a cage system with a 20x microscope objective lens, fiber adapter plate, and an eye piece (Figure 2.15). As commercial inspection tools cater to smaller diameter surfaces, this tool was constructed in-house to examine the full 2 mm face of the fiber. This tool helped to improve the quality and time efficiency of the polishing process.

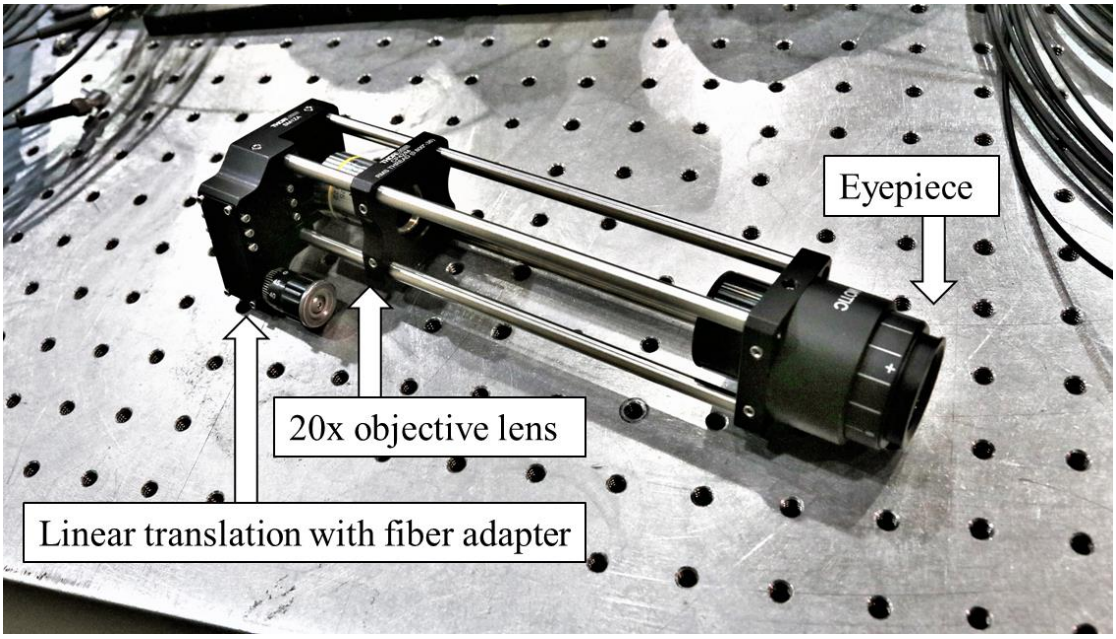

Figure 2.15 Custom fiber inspection tool, constructed in-house, to view full 2 mm of fiber face with 20x magnification.

CHAPTER 3: APPLICATIONS AND OUTCOMES

In this chapter we will cover several trial applications of FIZ in different pulsed power environments. Those environments include the Z machine, Mykonos, and the Applied B field on Z (ABZ) test chamber. For each environment, or application within the environment, a different configuration of the diagnostic was required. As well, different outcomes and lessons learned were obtained from each trial. Table 3.1 summarizes this information and the following sections present details of the environment, the configuration for that environment (or application within), the result, and the takeaways.

Table 3.1 Summary of Diagnostic Field Testing

Machine	Shot Type	Image Object/s	Image Type	Image Method	Imaging goal
Z	Helical instability (MagLIF)	Target liner	Self-emission	Single frame	Origin and characterization of low-density plasmas from the inner MITLs that potentially stimulate helical magneto-Rayleigh-Taylor (MRT) perturbations and reduce current delivery to the load
Z	Metallic coatings (MagLIF)	Target liner	Self-emission	Single frame	(Same as helical instability)
Z	Debris shield assessment (MagLIF)	Target liner	Self-emission	Multi-frame	Characterization of damaging debris
Mykonos	Hybrid x-pinch	Single wire load	Self-emission	Single frame	Characterization of plasma behavior under magnetic field compression
Mykonos	Hybrid x-pinch	Single wire load	Laser shadowgraphy	Single frame	Identification of density gradients and plasma flow patterns
Mykonos	Electrothermal instability	Stainless steel barbell	Laser shadowgraphy	Single frame	Identification of density gradients and plasma flow patterns
ABZ	MagLIF coil testing	MagLIF coils	Video with LED lighting	Multi-frame	Quantification of mechanical motion due to magnetic pressure

Table 3.1 Pulsed power platforms, configurations, and parameters for fiber imaging diagnostic field tests.

3.1: The Z Machine

The Z complex is in tech area IV, in the southeast region of Kirtland Air Force Base. A diagram of the facility (Figure 3.1) shows the layout and proximity of the Mykonos and the Z beamlet laser (ZBL) systems. About 200 technicians and scientists run Z experiments and operations. Shots are performed almost daily, and the shock can be felt in surrounding buildings. A picture of the Z highbay (Figure 3.2) provides some indication of the scale and complexity of the machine's operations. (The LOS30 screen room, highlighted in the photo, was the location of the camera used for this work.) The Z machine is ~33 m in diameter with three main stages to the system, the charge storage, pulse forming, and center

section. These stages are designed to compress energy in time and space to deliver mega amperes of current to the center, producing extreme pressures exerted on the target. Wall current flows to 36 banks, each with 60 capacitors (2.6 μF) for each generator. The Marx banks charge up in ~2-5 minutes, storing ~632 kJ of energy in each bank. Discharge happens in about 1.3 μs with ~180 kA peak current and ~90 kV from each generator[5].

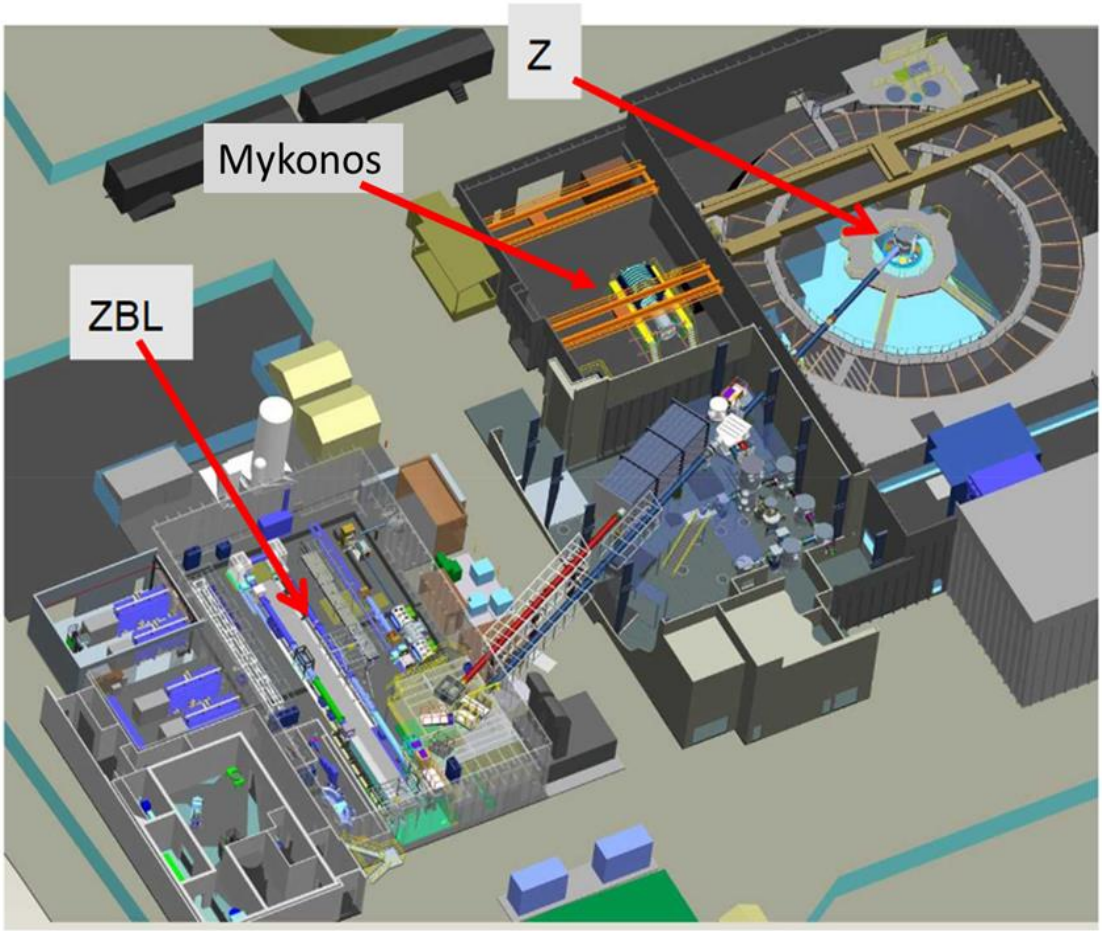

Figure 3.1 Adapted image of diagram of Z complex in tech area IV at Kirtland Air Force Base in Albuquerque, New Mexico. The Mykonos testbed and Z beamlet laser (ZBL) facilities are in close proximity to Z. ZBL is used for pre-heat during MagLIF shots, as well as radiography during ICF shots[50].

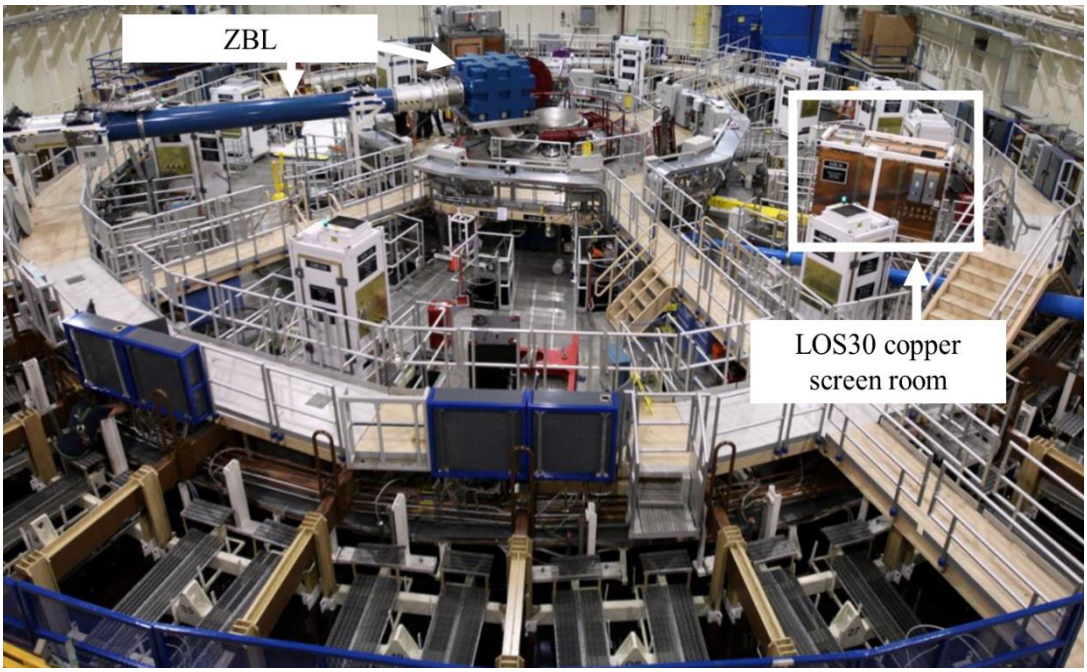

Figure 3.2 Adapted photograph of the Z machine highbay[50]. The camera, used for this project, was located in the LOS30 copper box screen room. Communication to the camera is diagramed in Figure 3.5.

In the pulse forming storage section, energy is compressed in time through a low-inductance network of water insulated storage capacitors, laser triggered gas switches, pulse forming lines (PFL), and transmission lines as detailed in Figure 3.3. Pulse forming networks are generally used for fast delivery of high power and the distinguishing components include the intermediate storage capacitor and control switches. The intermediate storage capacitor is able to discharge much faster than the Marx, allowing for quick high voltage charging of the PFL[47].

On Z, there are two control switches. A laser triggered gas switch, coupling the intermediate storage capacitor to the PFL, and a water switch, coupling the PFL to the output transmission line (OTL). The laser triggered gas switch is the last "command-triggered" switch in the PFL system. This switch dictates the accuracy and timing of current to the load, and due to the multi-channel Rimfire[48] design, is reported to reduce inductance. The gas and water switches, on either end of the PFL, employ a "double-bounce switching" technique which exploits charge time and line characteristics. First proven in 1978, the

double-bounce concept was described by Frazier and Ashby, as a two-stage set-up with a "charging pulse-line" and a "pulse-forming line", connected to a matched load[49].

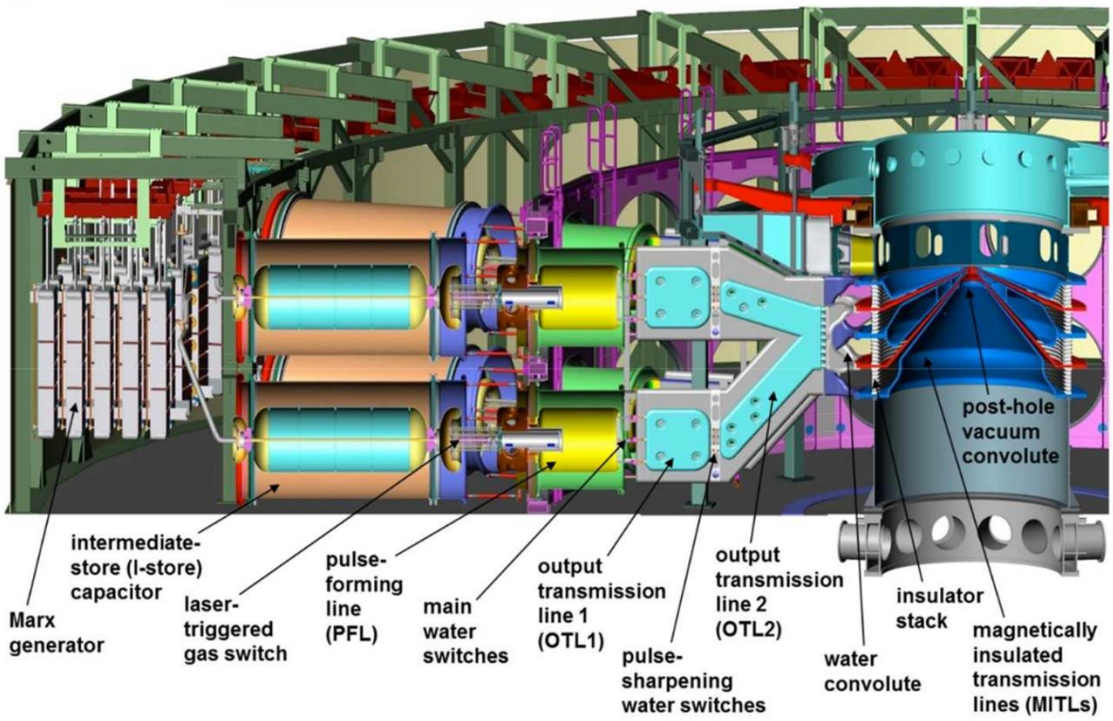

Figure 3.3 Component detail cross section of the Z machine highlighting specific components for charge storage, pulse forming, and transmission to the center section[50].

After pulse forming, power flows through water lines to a water convolute, transposing the electric field from horizontal to vertical at the center section. Further compression is achieved in the center section through 36 magnetically insulated transmission lines (MITLs) which can directly compress the energy up to 1μs. The center section transitions to a vacuum environment where robust barriers are needed to block off from the surrounding water section of the machine. Inside the center section is where the load hardware is installed. Figures 3.4-3.7 provide an example hardware configuration and some details regarding the MITLs. The blast shield is one of the few reusable components and it is delivered to the center section via overhead lifts. The blast shield helps contain some of the damaging shrapnel, as discussed in section 3.1.3. The floor of the center section

can be seen in the Figure 3.5 and it should be noted that the MITLs are located under that floor. The current feed to the load moves from the MITLs to a double post-hole convolute and on to the inner MITLs. Plasmas are noted in this current combining region[47].

The Z beamlet laser was initially developed in the 1990s at Lawrence Livermore National Laboratories in California as a prototype for the National Ignition Facility. Around year 2000 the laser was moved to Albuquerque and reconfigured to become Z-Beamlet. This laser aids in magnetized liner inertial fusion (MagLIF) pre-heating of the fuel filled target liner. The laser is timed with the Z shot within about 500 picoseconds and can be pulsed from 0.3 to 4 nanoseconds. The energy ranges from 4-6 kJ depending on the wavelength, either 527 nm or 1053 nm[50].

The Mykonos accelerator is also housed in the Z facility building. It is an active testbed for fundamental science and potential diagnostics for Z. More details about Mykonos are provided in section 3.2.

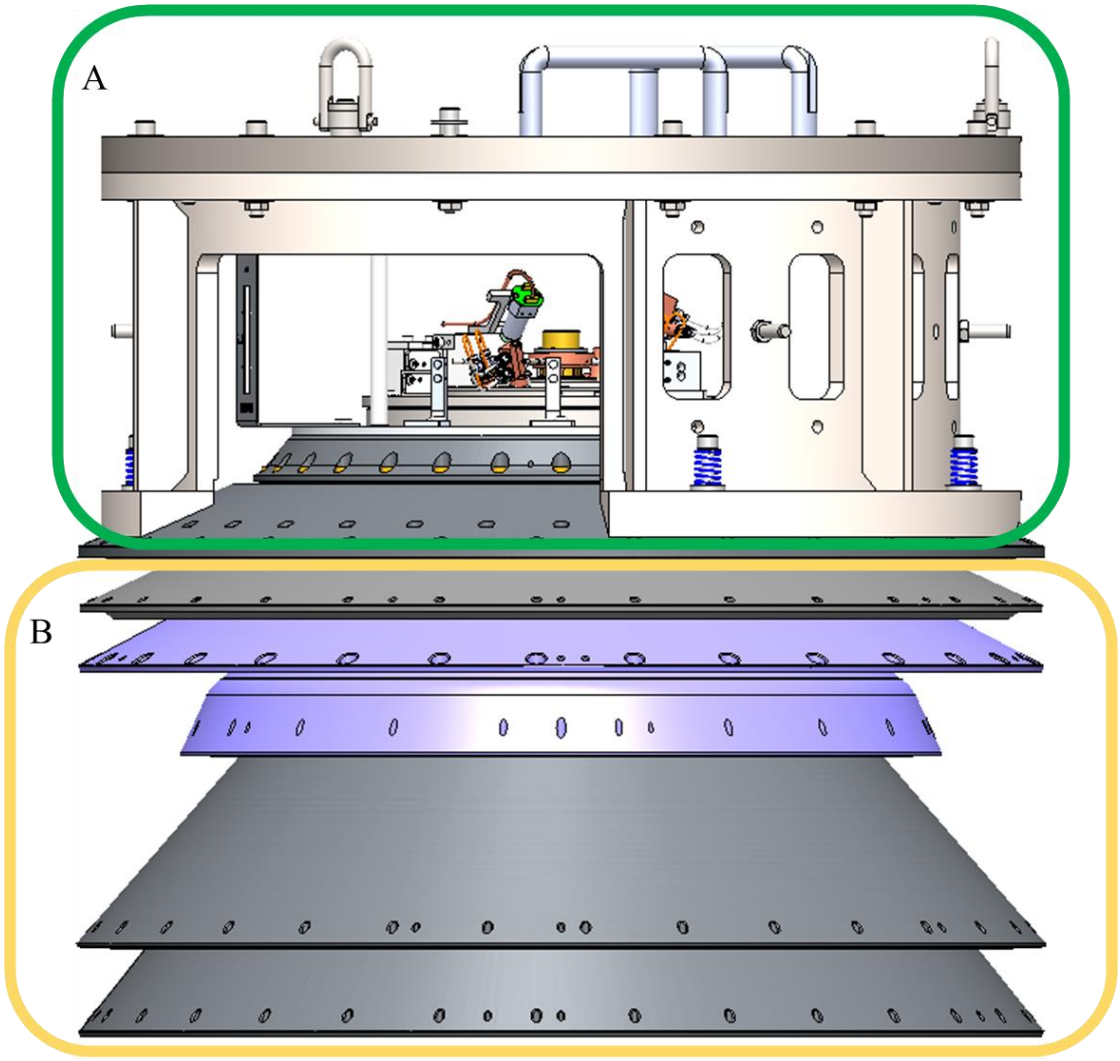

Figure 3.4 Example of the load hardware that is installed in the Z center section. The green boxed upper section (part A) shows the blast shield over the load and diagnostic instruments. The yellow boxed lower section (part B) shows the magnetically insulated transmission lines (MITLs) that provide current to the load.

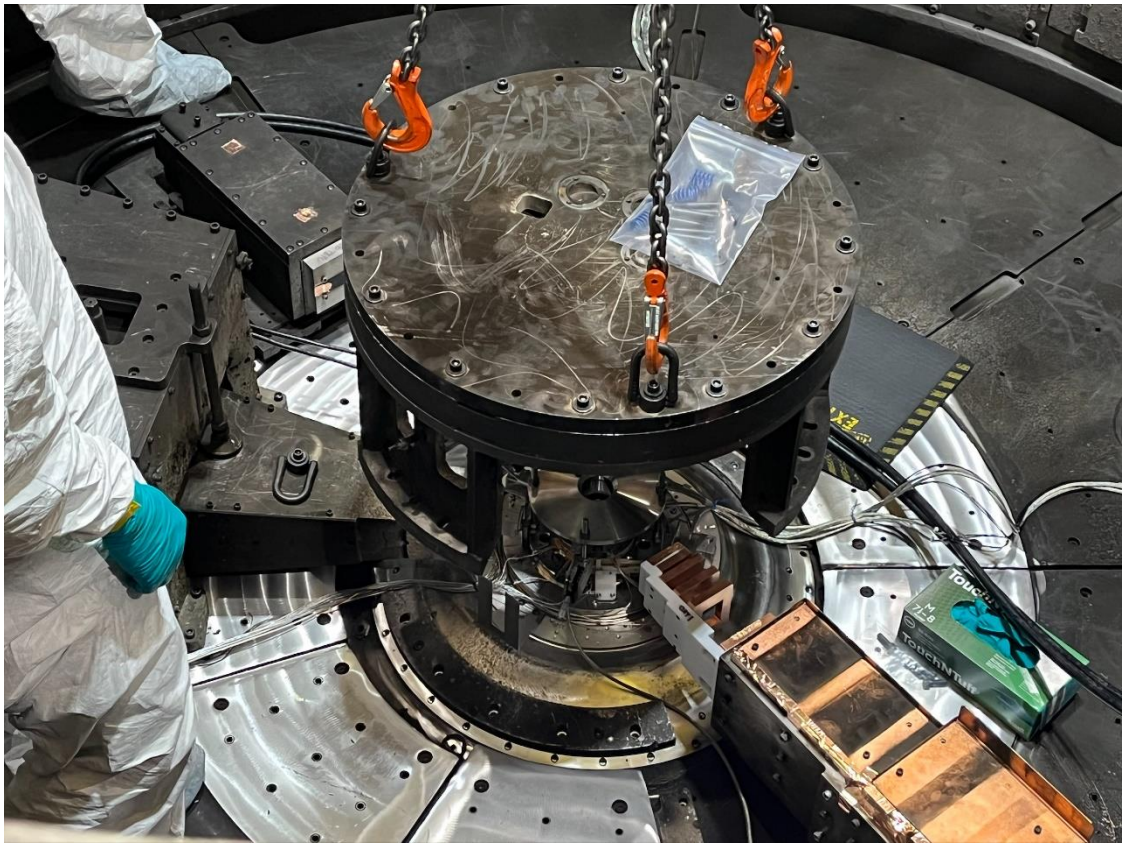

Figure 3.5 Photograph of the blast shield being lowered over the load hardware in the Z center section. Wires and cables, connected to many diagnostic instruments at the load, are strewn about the center section floor and MITLS are located underneath. See Figure 3.4.

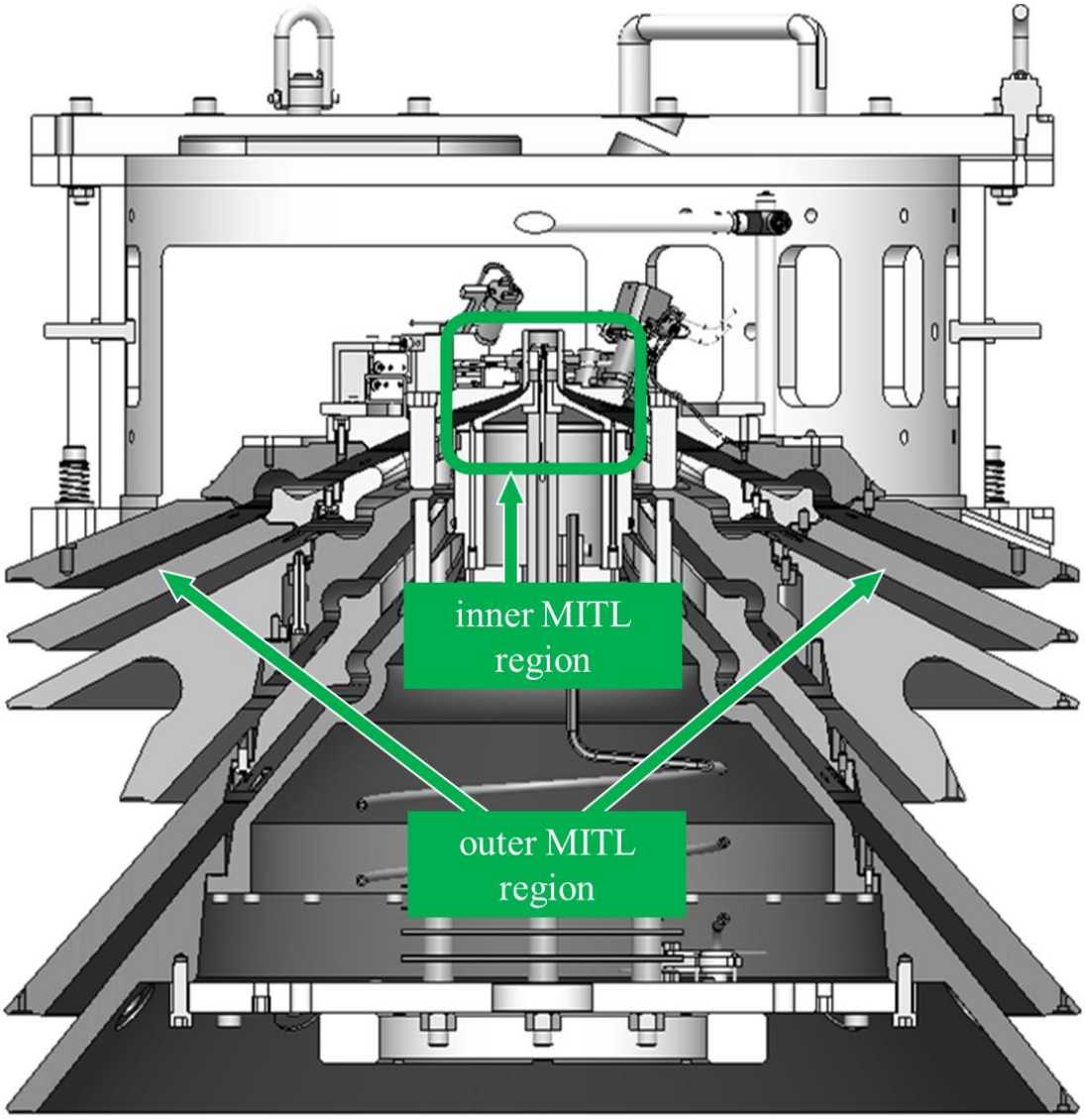

Figure 3.6 Cross section of the example load hardware (Figure 3.4) exposing the air gaps between the positive and negative MITLs and the inner MITL region (see Figure 3.7) and highlighting the outer MITL regions.

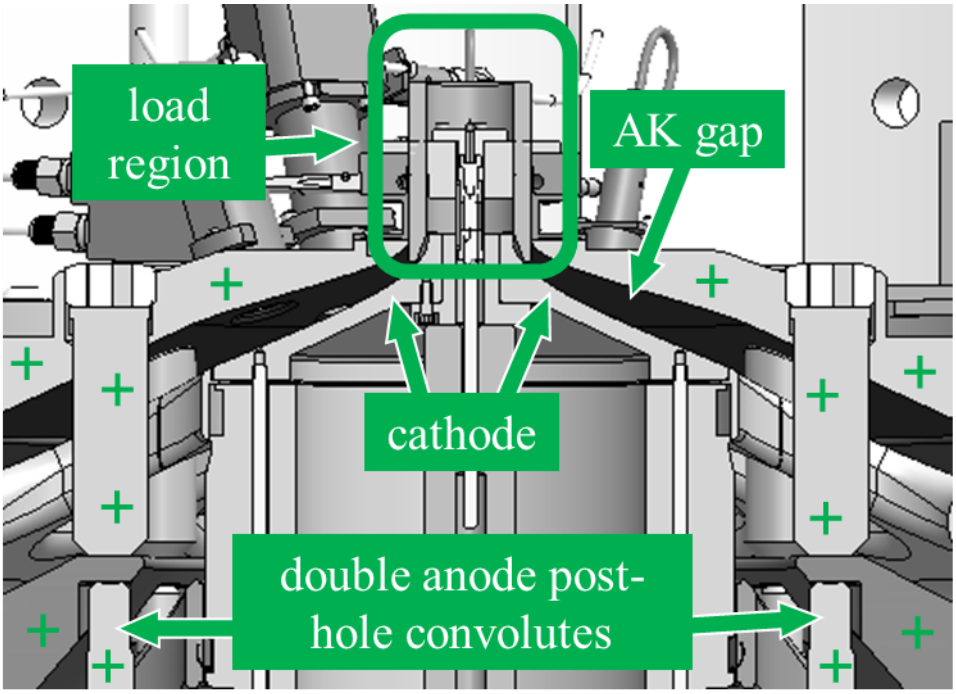

Figure 3.7 Detail of the inner MITL region indicating the anode fixtures with a green plus sign. The anode-cathode (AK) gap is where low-density plasma short some amount of current and potentially stimulate helical MRTI.

3.1.1 Fiber imaging on Z

For this project, the FIZ diagnostic was fielded on Z six times. Three different source side configurations (located in the Z center section) were developed to accommodate load hardware and desired line of site (LOS). Those source configurations will be reviewed within the corresponding application sections that follow. The sensor side of the diagnostic was housed in the LOS30 screen room located in the Z highbay, as shown in Figure 3.2. An overview of the camera setup is provided in Figure 3.8 and a diagram of communications to and from the camera is provided in Figure 3.9. This communication scheme and the shown camera setup were used for all trials on Z.

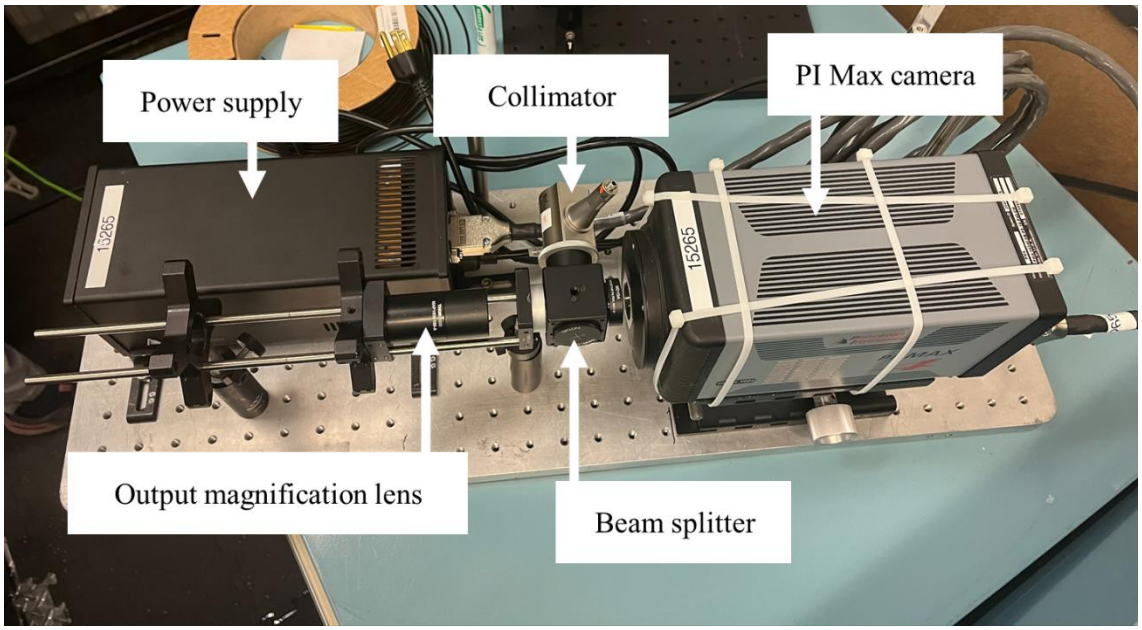

Figure 3.8 Overview of sensor side camera system mounted to an optical breadboard for transport. The crucial components are labeled.

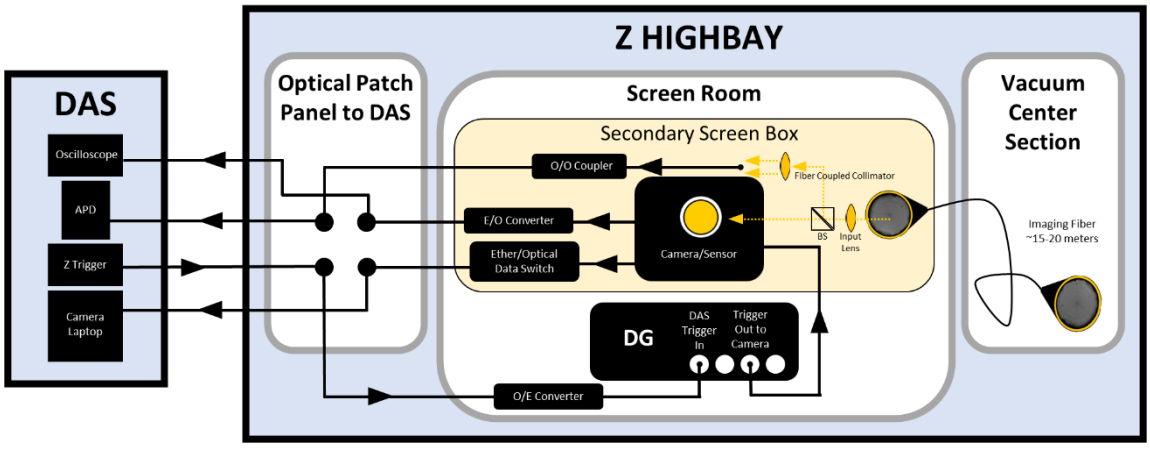

Figure 3.9 Communication diagram for Z shots with the camera located in LOS30 screen room in the Z highbay. An intermediate optical patch panel is used for fast signal travel between long distances within the Z facility. Acronym definitions from left to right: DAS – data acquisition system, APD – avalanche photo diode, O/O – optical to optical, E/O – electrical to optical, DG – delay generator, BS – beam splitter. Self-emission light travels from the center section through the imaging fiber to the beam splitter sending 92% of the signal to sensor and 8% of the signal to the APD.

Most communication lines were pre-established in the screen room, but the imaging fiber had to run each time. The imaging fiber was continuous from the center section and was consequently destroyed during each shot. Each imaging fiber was secured through a vacuum kwik-flange (50 mm KF, Figure 3.10) that connected to a chamber port at the vacuum wall. Each potted fiber underwent seal testing to ensure sufficient performance under vacuum. Through this testing, negligible leaking through the fiber was determined but within operating range.

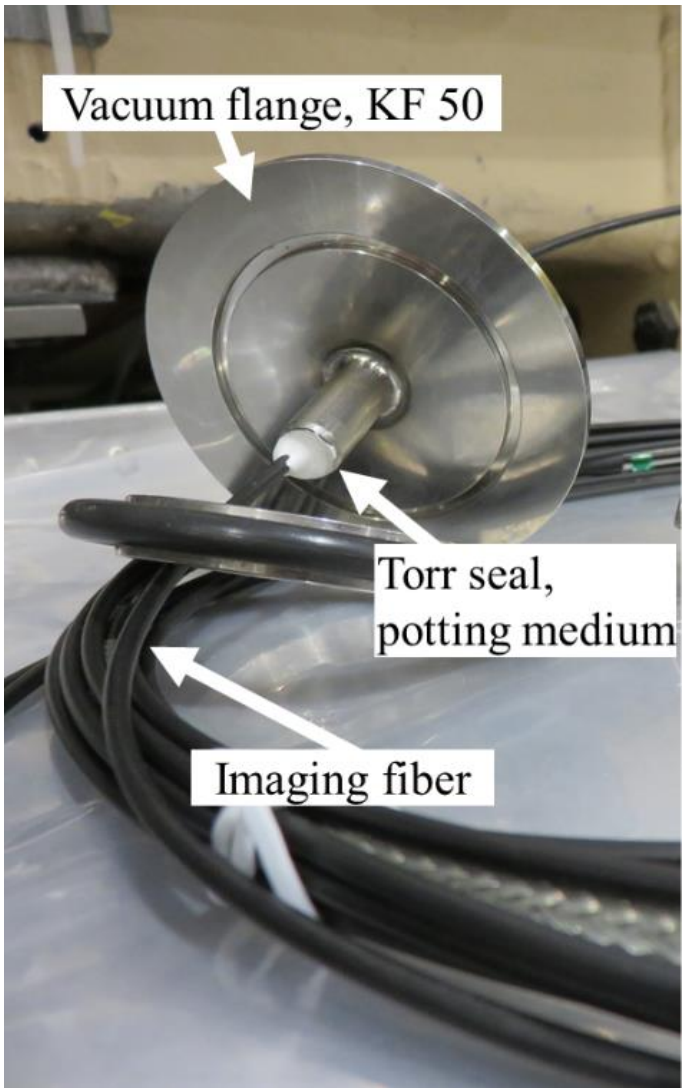

Figure 3.10 A new imaging fiber, potted in a vacuum flange, was installed for each Z shot.

Based on the EMI testing performed previously, it was determined that the LOS30 screen room in the Z highbay was not sufficient to attenuate EMI. Construction of a custom screen box (Figure 3.11a) was needed to shield the camera and switches from passing energy that could disrupt data transfer. The five-sided screen box was sealed at the base with conductive copper tape (and a little blood!), creating an electrical path to the aluminum shelf.

For isolation and transport, key components for the sensor setup were secured onto a large optical breadboard. As shown in Figure 3.11b, the board was covered in gaffing tape to avoid reflections onto the open sensor, and foam padding was placed under the board to reduce vibration and increase electrical insulation. The camera and the camera power supply consume most of the space, but the optical configuration (including the imaging fiber, magnifying lens, beam splitter, and collimator) neatly fits to the side of the power supply. The ether/optical switch rest at the far end, behind the camera, and a free-standing computer fan was installed on the side of the camera to support cooling. The screen box was designed to fully enclose the board without contact.

A 92:8 visible range beam splitter (BS), coupled with a one-inch collimator (BS to C in Figure 3.11b), was used to record the incoming self-emission signal. 92% of the signal went to the camera sensor and 8% of the signal went through the collimator to an SMA silica fiber optic which traveled to an avalanche photo diode (APD) located at Z's data acquisition system. Later on, this information was compared with the camera trigger to understand the timing of the trigger in relation to the emission. Because the light intensity was unknown, neutral density (ND) filters were employed at the beam splitter to protect the camera sensor. For the first shot, a 10x attenuator was also placed on the APD but proved to be unnecessary and was removed for later shots. While the ideal ND was never determined for camera, ND = 1 (10% transmission) was found to be an adequate filter for the APD and remained on the collimator for the next shots.

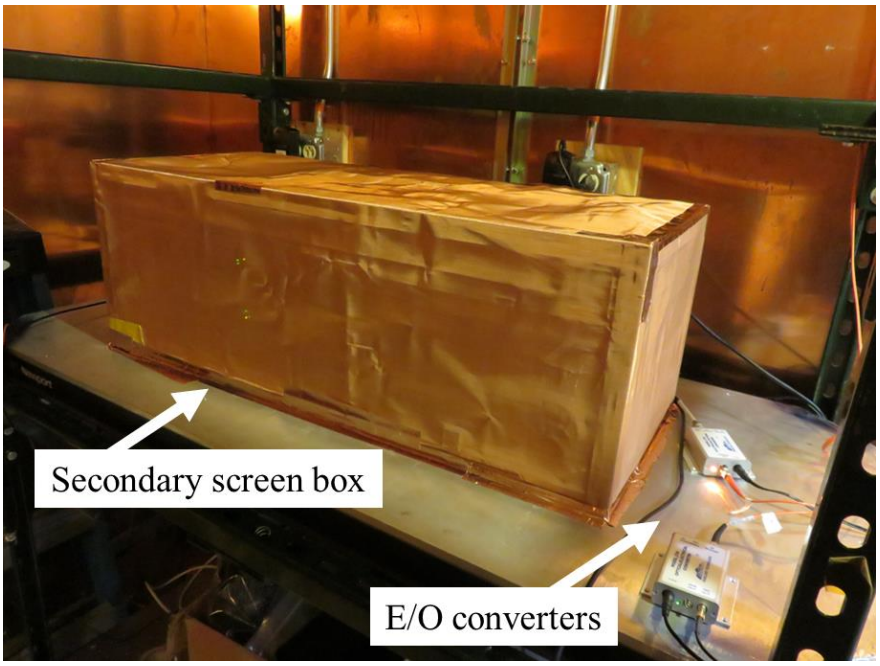

(a)

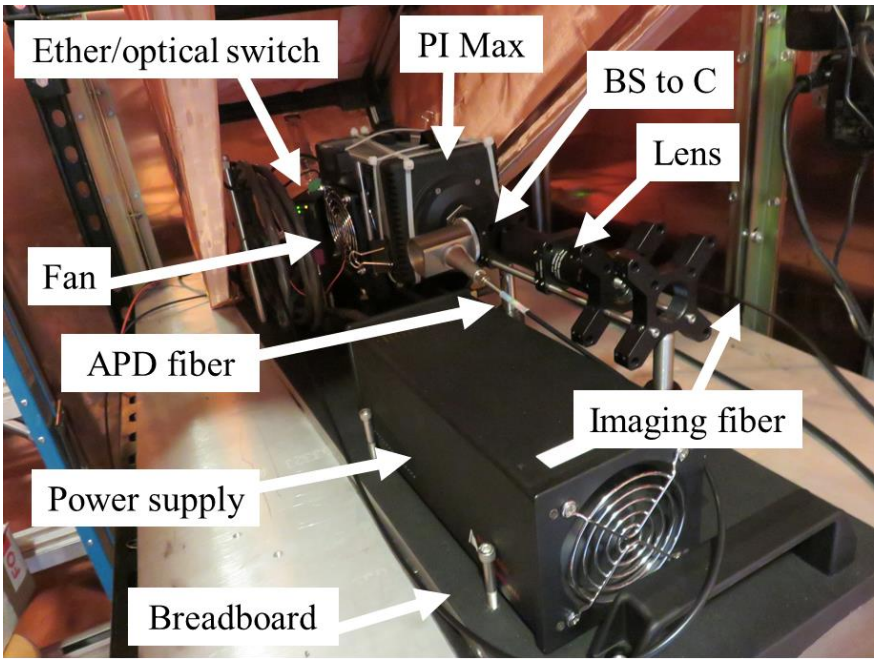

(b)

Figure 3.11 Inside LOS30 screen room, a second screen box was used (a). Under the screen box was the sensor end of the diagnostic (b) as also described in Figure 3.8.

3.1.2: MagLIF

In MagLIF, there are three stages to achieve thermonuclear conditions. First, an axial magnetic field is applied via Helmholtz-like coils installed concentric to the target. Second, the target undergoes laser pre-heating via Z beamlet. Last, the target is imploded via a large electrical current and is quasi-adiabatically heated to thermonuclear conditions. The applied axial magnetic field enhances the trapping of charged fusion particles while reducing thermal conduction losses to the liner during the implosion. Hydrodynamic instabilities such as the Magneto Rayleigh-Taylor (MRT) instability challenge further advancement and it is a goal of this imaging diagnostic to provide additional insight into plasma behavior during these shots.

This section is organized into two sets of MagLIF Z shots, helical instability and metallic coatings. The key difference between the sets of shots is the target liner and the suite of diagnostics. Between the two sets, FIZ was fielded five times and, despite the lack of data, much was learned from the preparation and installation process. Two different source side configurations were designed and implemented. The camera gate on the PI Max varied between shots but the gain was always set to 1x.

3.1.2.1: Helical instability

As discussed in the motivation, it is hypothesized that low density plasmas flux compress the applied axial magnetic field to large values. This phenomenon is suspected to modify the MRT instability into a helical shape. In general, low density plasmas are not observable in x-ray radiographs (chapter 1, Figure 1.1); therefore, we need diagnostics in the visible range to study their dynamics. On Z, helical instability shots are one hardware configuration designated for this purpose.

These helical instability studies were the first Z attempts for the FIZ diagnostic. The two shots were Z3669 and Z3670. Due to space limitations around the load hardware, it was decided to incorporate an aspheric Thorlabs lens (model 354240-A, FL = 8 mm) embedded in the existing structure. To do this, the mechanical engineer on the team designed a mounting scheme to install the lens and fiber and focusing capability. Figure 3.12 shows the 3D printed parts (A-C) that were designed and the installation concept to include a commercial translation stage. Part A (two purple pieces) pressure fit around the

lens to secure it approximately 2 inches away from the target. The two pieces were then glued to the metal support structure, permanently embedding the lens in the hardware. Part B, the tubular extension, held the imaging fiber which was also glued into place and had to be attached later to the translation stage. Part C was a mounting bracket that slide over an existing threaded rod and was suspended vertically between two lock nuts. The translation stage was screwed to this printed bracket and the fiber holder screwed to the translation stage. By adjusting the translation stage, the distance between the lens and fiber face could be optimized.

During installation, the remote camera operator was able to live-view and communicate via radio with the installer. While installation was successful, focusing the fiber and taking reference images proved to be challenging. As demonstrated in Figure 3.9, it was difficult to in-the-moment interpret the components in view. The image was rotated, blurry, poorly lit, and we had no prior reference image to compare. After the shot, the mechanical engineer on the team put together a comparison with the SolidWorks® model to help orient and describe the parts captured in the pre-shot image. The target has a 5.6 mm diameter so a FOV estimate is about 1 cm for this pre-shot image.

For these two shots a signal was received each time (meaning the camera gate was recorded at DAS) but the signal was either too low and overwhelmingly noisy, or too high and saturated the sensor. The camera gate was 1.28 ns and 20 ns for the respective shots and triggering was determined through complex timing calculations.

From these first trials, the following takeaways were noted and incorporated into the planning of the next shots.

- Timing, especially with fast gates, is incredibly complex and particularly tricky with unknown light intensities.
- Embedded lenses are a successful method to increases LOS access, however, positioning options (xyz at minimum) would be ideal.
- Reference fiber images of the target region are needed prior to center section installation to interpret viewing area during installation.
- Bright diffused lighting of the target (or viewing area) is needed for fiber viewing and focusing during installation.

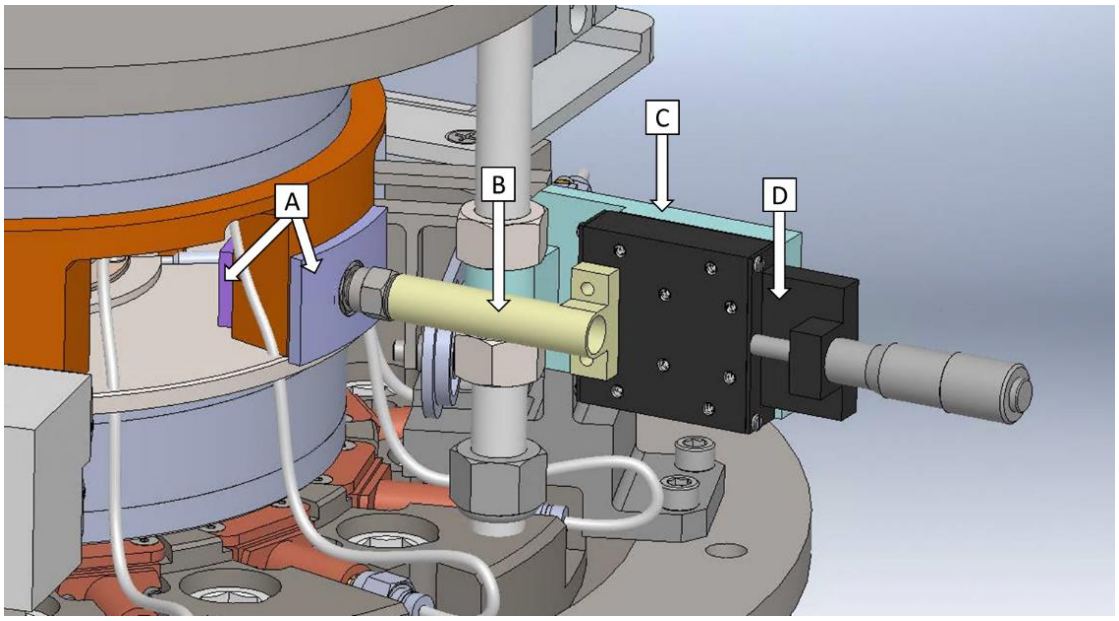

(a)

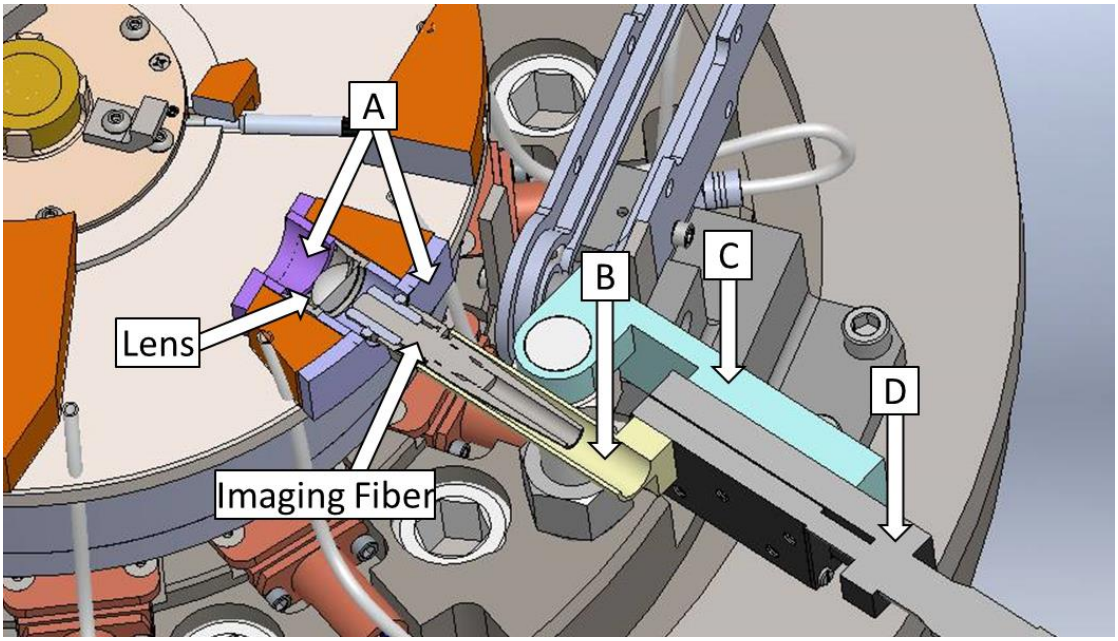

(b)

Figure 3.12 Source side lens configuration for two helical instability MagLIF shots. An aspheric lens (FL = 8 mm) is embedded into the magnet support structure of the load hardware and 3D printed parts (A-C) secure the lens and imaging fiber. (a) Finished installation including a commercial linear translation stage to focus the image onto the fiber face. (b) Cut away of the setup to reveal the embedded lens and placement of the imaging fiber.

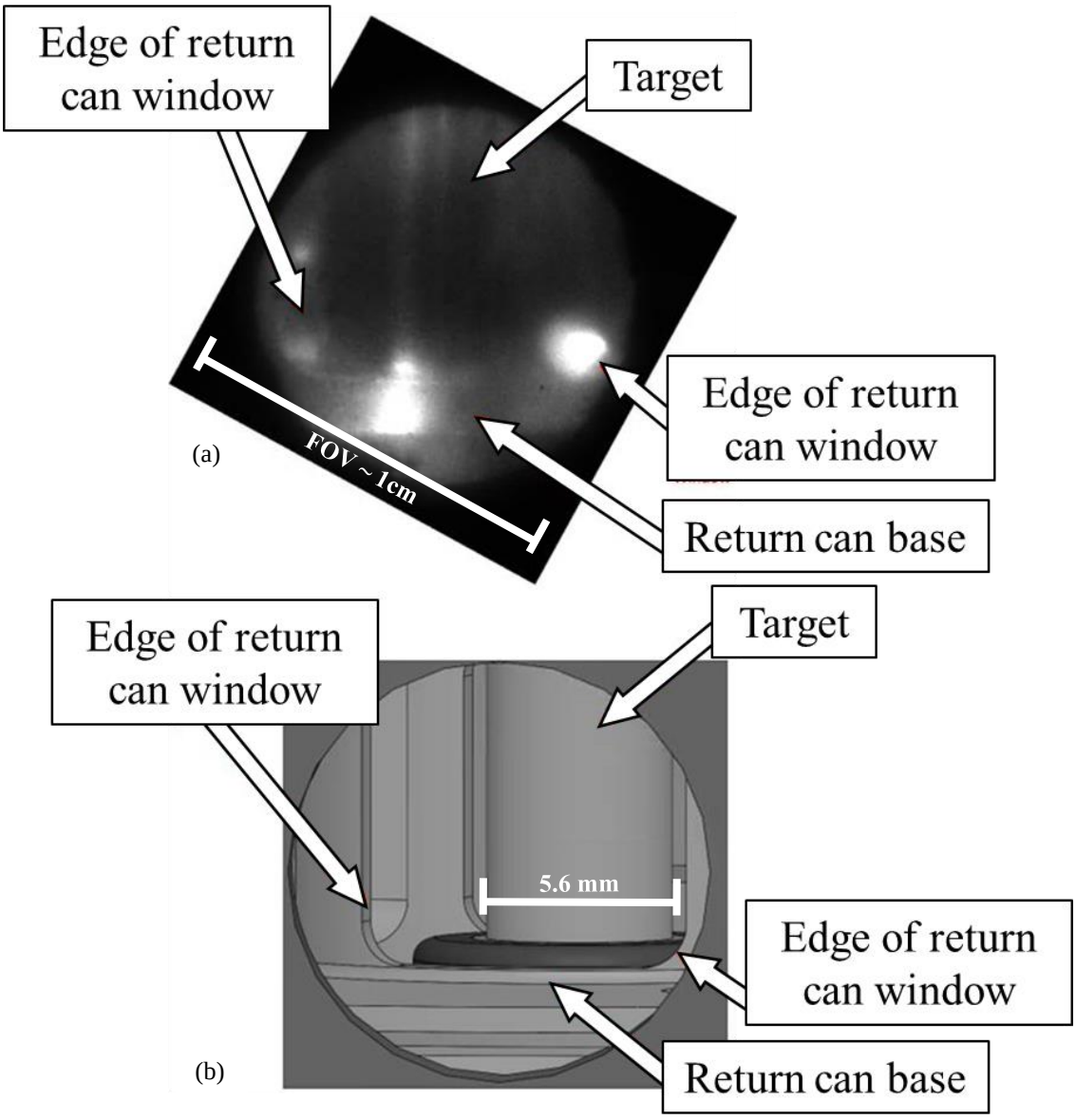

Figure 3.13 (a) Example of pre-shot reference image of the 5.6 mm target during center section installation. Poor lighting and unrefined polishing contribute to the fuzzy image quality. FOV is estimated to be about 1 cm. (b) Estimated comparison with SolidWorks® load hardware model to help interpret reference image.

3.1.2.2: Metallic coatings

This next series of three shots was actually two metallic coating and one debris assessment, Z3679, Z3680, Z3681. However, the source side FIZ configuration was the same for all three sequential shots, with the same 12.5 cm distance between the target and lens, see Figure 3.14. (A second debris assessment shot, with a different FIZ configuration is discussed in the next section.) Again, the key difference between the shots was the target liner and fielded diagnostics. The two metallic coating shots were beryllium liners with an exterior aluminum finish, and the debris shot was just a standard beryllium liner. All three shots were MagLIF with the same line of site as shown in Figure 3.15.

With regard to metallic coating studies, it is hypothesized that an appropriately chosen coating, over the standard beryllium liner, could mitigate the electrothermal instability postulated to seed MRT. Compared to dielectric coatings, a metallic coating will implode with the target and potentially limit plasma at a larger radius. This can lead to redistributed current from stagnation of the target, reducing the ram pressure and therefore the fusion yield. These specific experiments (Z3679 and Z3680) tested an ultrapure aluminum coating over a beryllium liner.

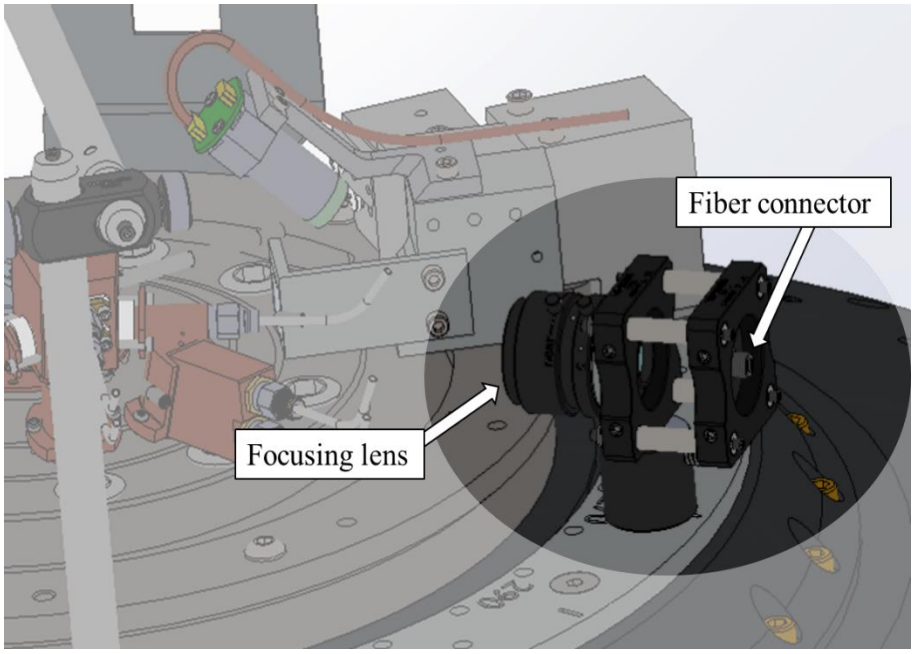

Figure 3.14 FIZ configuration on the aperture ring of the load hardware. Distance is 12.5 cm between the target and the lens. Same setup was used for the three shots described in this section.

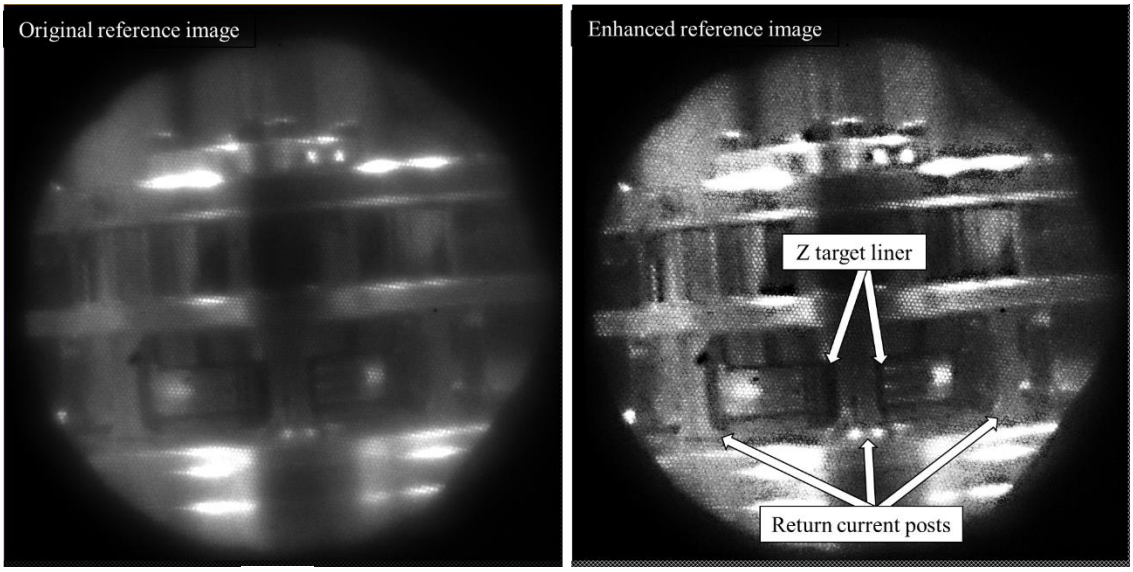

(a) (b)

Figure 3.15 (a) Reference image taken with room lighting before center section installation. Image provided the expected focus and FOV (~5 cm) and served as a useful comparison during installation. (b) An enhanced version of the reference image highlights the fiber pixels and provides better contrast to identify the structures in the image.

The image of the target in Figure 3.15a was taken with room lighting prior to installation in the Z center section. The input lens was the wide-angle (model M0814-MP2) described in Table 2.1. The FOV is approximately 5 cm and the resolution was predetermined (given the known distance) to be about 280 μm. This image served as a comparable reference to help orient the camera operator during installation and alignment. Figure 3.11b is provided to highlight the fiber pixels and structures of the target in view.

Reference images taken during installation on Z3679 were not useful as harsh flashlight lighting produced intense reflections that saturated sensor pixels. Some examples are provided in Figure 3.16. Consequently, the experience reiterated the need for bright diffused lighting for installation viewing purposes.

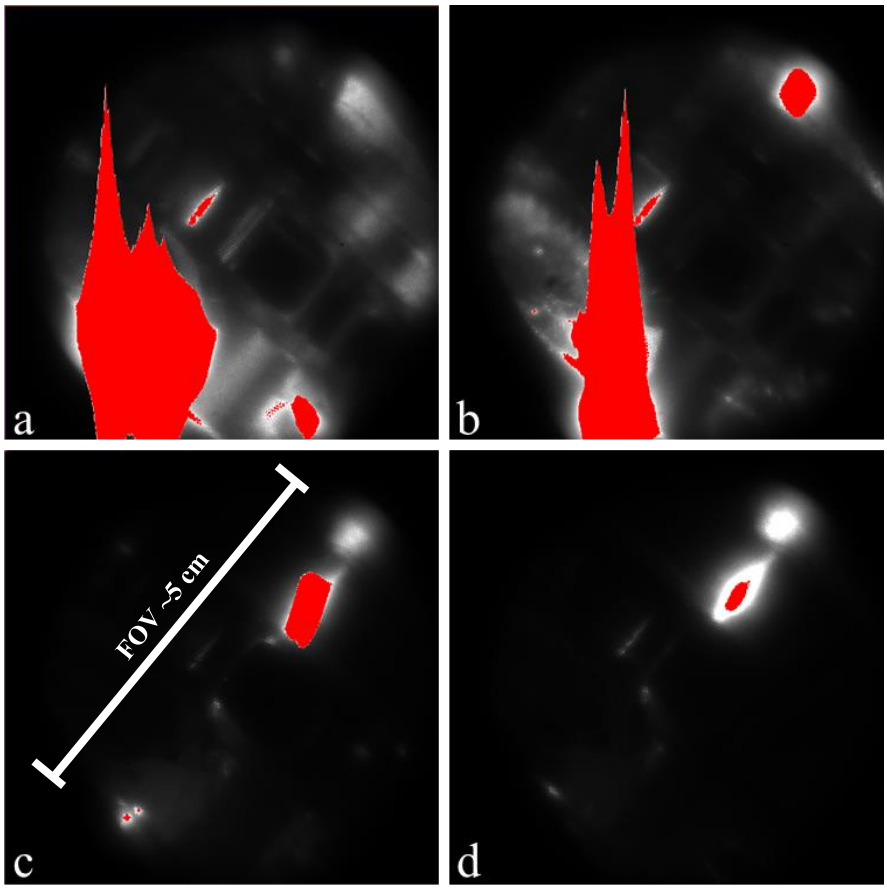

Figure 3.16 Examples of reference images taken during center section installation of metallic coating shot. Red splatches indicate saturated sensor pixels caused by intense flashlight reflections off the metal hardware. Comparing (a) with the 3.15a, the fiber is rotated, and it is still difficult to determine top and bottom of the target.

For the first shot, Z3679, there was no ND filter on the camera, gate was 10 ns, and the sensor saturated. For Z3680, there was an ND = 1 (10% transmission) filter on the camera, gate was 1.28 ns, and the sensor only captured noise. For the last shot, Z3681, there was an ND = 0.5 (32% transmission) filter on the camera and gate was set to 2 ns. Data from the camera to the laptop did not transfer during this last shot. The camera was known to have triggered given the captured signal at DAS. This data transfer failure was unexpected and seemingly unavoidable. This issue had not been experienced since prior EMI testing and was thought to be remedied with the secondary screen box. Lessons learned from these shots are as follows.

- Having the PI Max ICCD camera in the Z highbay is problematic regarding data transfer. The camera will need accommodation in a different location to be used on future Z shots.
- More work is needed to narrow in on a gate range and filter setting for the camera.
- During installation for the second shot, the imaging fiber was damaged and was replaced with the fiber designated for the third shot. Fortunately, in-house capability to repair the fiber had been established, so there was no delay in having a third fiber ready for the next day. However, a fourth (extra) fiber would have been prudent to have on hand.

3.1.2.3: Debris shield assessment

As described by Yager-Elorriaga *et al.*[8], the explosive events that occur in the Z center section produce copious amounts of destructive material. The material can be characterized as soot, spray, particulate, and bullets[50]. Each category has a size distinction with suspected corresponding damage such as to the vacuum system, detectors, or chamber walls. It was the goal of this application to try and image this material as it flew from under the blast shield. This was a utility expansion for the diagnostic that was not previously conceived but proved to be a natural progression.

As Figure 3.17 illustrates, the FIZ source side assembly was placed on top of the blast shield with the lens over hanging the edge. The imaging fiber was connected at the top of the assembly and the lens tube shown represents the wide-angle lens (model M0814-MP2) described in Table 2.1. As debris moves at a slower time-scale than plasma, the multi-frame Phantom® VEO camera could be used for this application. The specifics of this camera are described in section 2.2.2 but in general this device has a longer gate, 1 μs, and was used with a 10,000 frames per second frame rate. The camera was located in the LOS30 screen room in the Z highbay, without a secondary screen box. The communication scheme was similar to that in Figure 3.9, minus the beam splitter and APD.

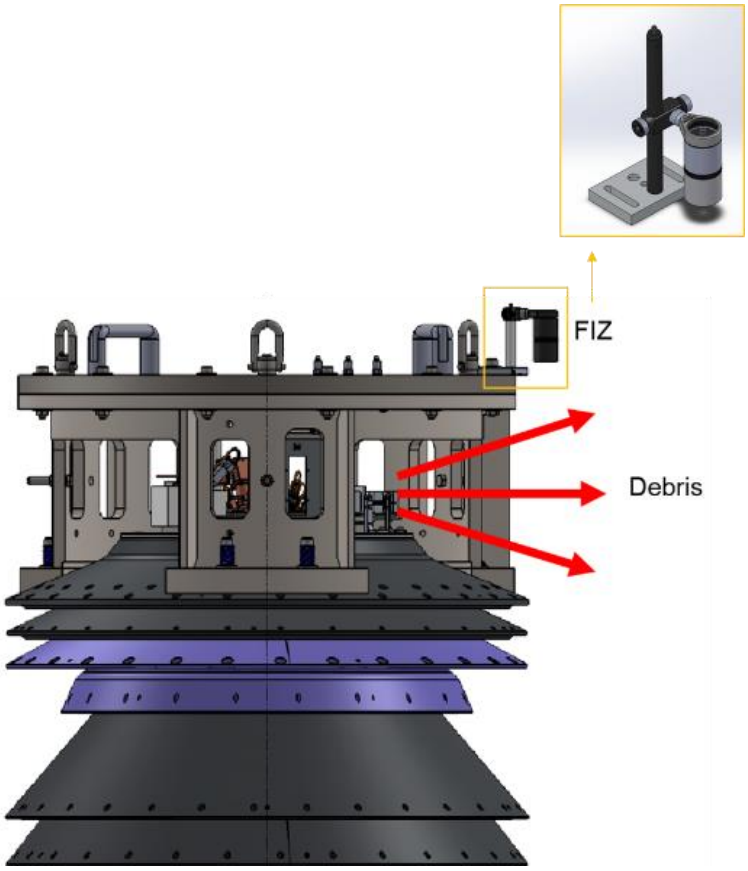

Figure 3.17 Adapted image showing FIZ configuration for debris assessment shot with the lens assembly on top of the blast shield looking down to view flying shrapnel. Detail shows a mockup of the assembly using a lens tube to represent a lens configuration[8].

Unfortunately, data was not captured from this shot due to a significant malfunction in the Z machine which halted operations for several weeks. Nevertheless, key takeaways from this experience were as follows.

- Need bright/diffused lighting for viewing and focus during installation.
- Need illuminated fiducial and fiber translation to help optimize the fiber distance and focus the lens.

This last takeaway led to identification of a bright battery-operated LED flashlight that was small enough to bag and handle in the center section. A paper USAF resolution target could be taped to the front (Figure 3.18) providing the illuminated fiducial that was found to be needed during installation. As well, a simple linear translation system was

constructed with commercial optical parts and a 3D printed part (Figure 3.19). This solution provides quick and inexpensive translation for future configurations.

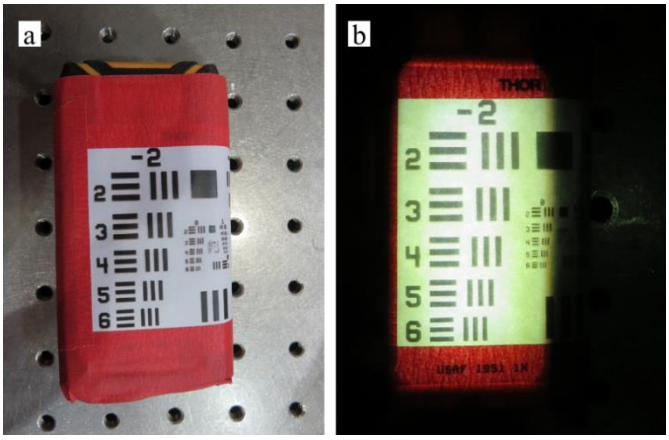

Figure 3.18 Illuminated fiducial can be used to help focus FIZ system for imaging flying debris on future Z shots. A small LED flashlight is outfitted with a paper USAF resolution target providing a bright well defined source during installation.

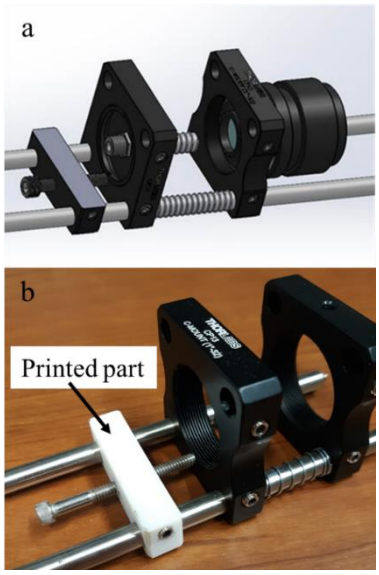

Figure 3.19 In-house linear translation system using commercial optical cage components and one 3D printed part. (a) Shows the full design with the fiber connector plate and lens in place. (b) The actual assembly with printed part deployed.

3.2: Mykonos

Sandia's Mykonos accelerator is a linear transformer driver (LTD) voltage adder capable of 1 MA and 100 kV in ~100 ns rise time. Five high-current modular cavities are 3 meters in diameter and are water insulated from the vacuum section. Interchangeable vacuum chambers make this testbed ideal for a variety of fundamental pulsed power experiments. It is often used to assess new diagnostic concepts or techniques for the Z machine.

The high-current modular cavities that enclose the LTD design, employ numerous gas switches, capacitors, and insulators to achieve single-stage pulse compression. The paper by Mazarakis *et al.*[21], provides excellent detail of how the cavities are constructed but a high-level description includes the following. Each cavity is a hollow ring containing 40 "bricks". A brick consists two series capacitors with a gas switch in between. The bricks are insulated from each other with oil and the cavities are connected in series to increase total charge voltage. Currently, Mykonos is configured with five cavities and charge voltage is limited to 90 kV to prevent arcing.

3.2.1: Hybrid x-pinch

Recently, hybrid x-pinch (HXP) studies were fielded on Mykonos. These studies were prompted by the work of Myers *et al.*[51], where inductively driven transmission line results led to testing HXP x-ray emission. HXP is a simplified and reproducible single-wire configuration, compared to the standard two-wire x-pinch. As shown in Figure 3.20, instead of crossing wires, two electrode cones hold a connecting thin wire which produces a z-pinch plasma with soft x-ray emission[52,53].

For these HXP shots, the FIZ was installed as a ride-along diagnostic. To work around other diagnostics on the experiment, an image path was constructed using a supplemental 400 mm focal length lens[54] to create the image. Figure 3.21 illustrates the basic path (not to scale) from the center load to the fiber face, ~1.7 m total length. The wide-angle lens[41], used previously, coupled the image to the fiber face. Images were transmitted through 80 meters of fiber to the PI Max ICCD; 2 ns gate, 1x gain.

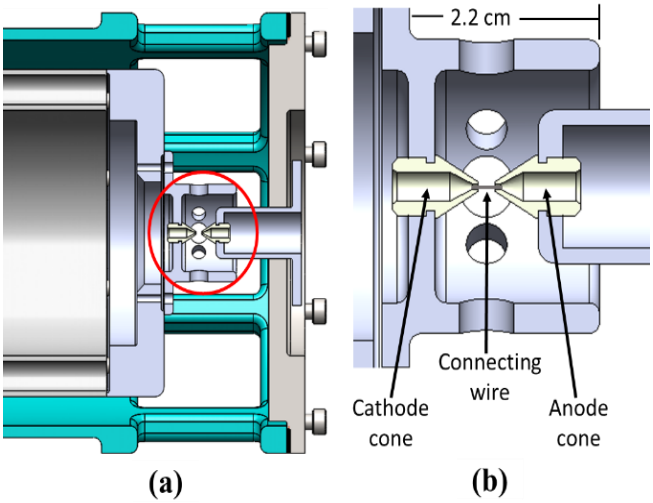

Figure 3.20 Cross section of hybrid x-pinch experimental hardware on the Mykonos accelerator. (a) Primary anode/cathode configuration for current delivery to the wire load. (b) Detail of connecting wire load. The wire is typically ~100 μm in diameter, the cone tips are 1 mm in diameter, and the electrode gap is nominally 2 mm.

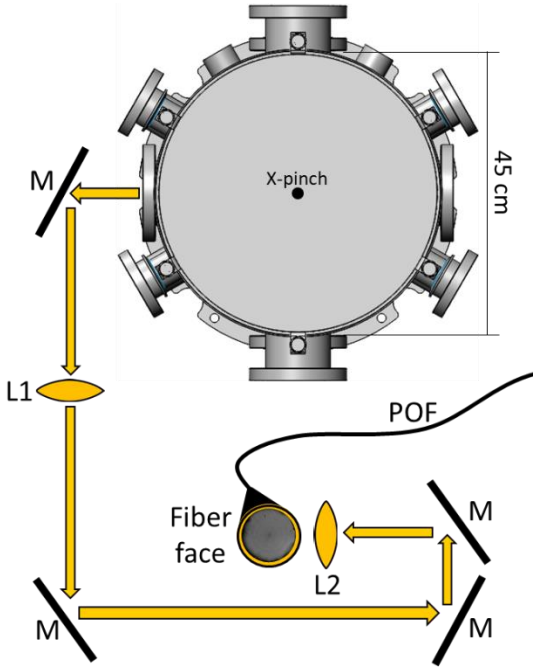

Figure 3.21 Diagram of image configuration from the center load to the imaging fiber (not to scale). L1 (fl = 400 mm) created an image collected by L2 (wide-angle lens, see Table 2.1) that coupled to the POF. The image was transmitted through 80 meters of POF to the PI Max 4 camera.

The reference pre-shot image in Figure 3.22 shows the approximated position and scale of the 1 mm diameter cone tip, 100 µm wire and estimated 3 mm FOV. The overlap image provides insight into the visible plasma expansion relative to the wire. Interestingly, the plasma does not appear axially symmetric with the wire and concentrates toward the cathode. The lack of symmetry could be a point of interest for future work.

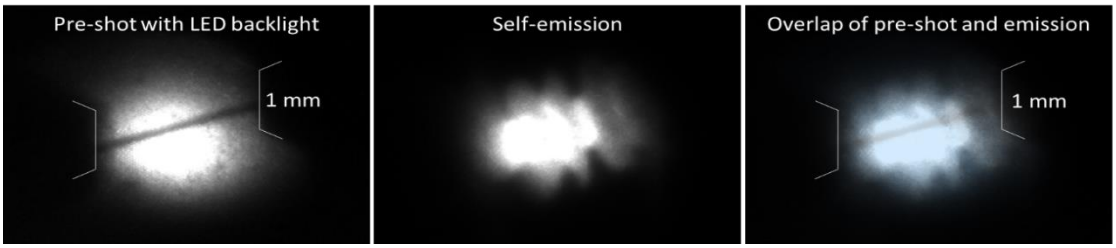

Figure 3.22 Images from a molybdenum hybrid x-pinch on Mykonos. Pre-shot (left), self-emission (center) without a backlight, and a simple overlap of the two (right). The overlap image was created by placing the pre-shot image at 60% transparency over the emission image from the shot. The wire is ~100 µm in diameter with a nominal 2 mm gap between the cone tips.

During these HXP studies, two different wires were tested, molybdenum and nickel, each ~100 µm. Plasma formations were captured at different times during the rise of the current pulse (Figure 3.23). While cone and wire position slightly varied, lens position and image path was constant for all three instances. Using the 100 µm wire as a spatial fiducial, a 25 µm feature could be resolved. As a result, we estimate the resolution to be at least 25 µm.

Observed from these images is the early electrode plasma concentrating over time to the brighter round pinch forming at 640 kA. The image suggests the presences of a characteristic z-pinch sausage-like instability. Also, the structure of the plasma seems to vary a bit, although more frames are needed to fully examine the temporal dynamics. In general, nickel appears a bit brighter in the visible wavelengths.

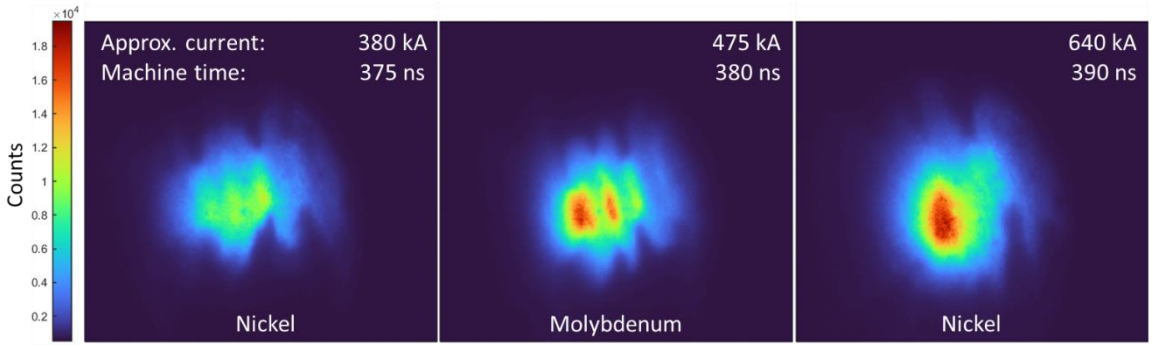

Figure 3.23 Self-emission images of hybrid x-pinch studies on Mykonos. Nickel and molybdenum wires were ~100 µm in diameter. Peak current was ~825 kA at 430 ns.

3.2.2: Shadowgraphy

A shadowgraphy system installed at Mykonos uses a 532 nm backlighting laser with a pulse width of 170 ps. A complex open optical path splits and delays the beam to pass through the target region producing an image onto multiple camera sensors. The CMOS cameras used in this system are Canon EOS rebel T7 and they have an approximate 1 second exposure time.

One camera path was intercepted to insert a FIZ setup. Figure 3.24 shows a sample of the configuration and image path leading to the FIZ input lens. The imaging fiber was focused along this path and transmitted the image through a short fiber to a lens coupled onto a Canon sensor. The system successfully captured plasma formations during the HXP studies. In Figure 3.25 a pre-shot of the cones and wires is shown for reference and an image during the pinch show the plasma formations at 380 ns machine time.

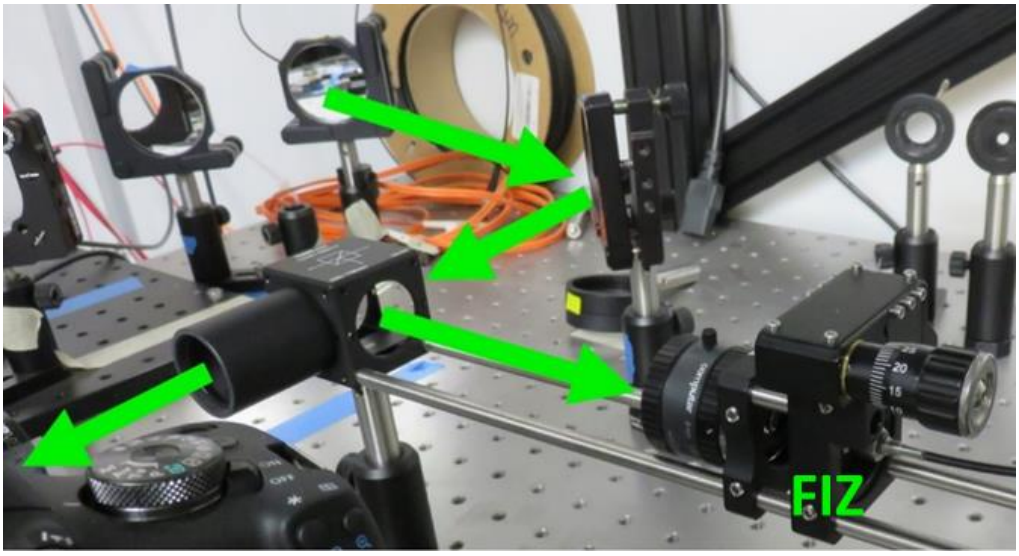

Figure 3.24 Sample of the image path to CMOS Canon cameras and FIZ system. The imaging fiber was coupled to a lens magnifying the image onto a Canon sensor.

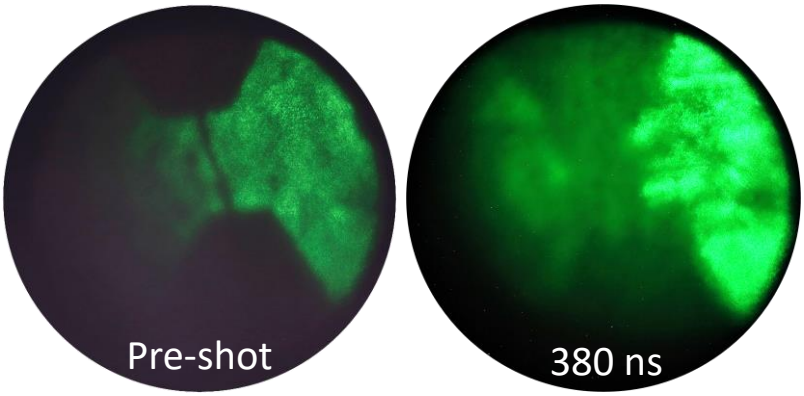

Figure 3.25 Images from the FIZ system installed along the shadowgraphy image path at Mykonos. Pre-shot image shows the x-pinch cones and 100 μm wire. FOV is estimated to be about 6 mm. Shot images at 380 ns machine time shows plasma formations during the pinch.

3.3: Applied B Field on Z System

At Sandia, a small, isolated vacuum chamber is equipped with a pulsed power system to test the magnetic coils fabricated for MagLIF shots. The system is known as Applied B field on Z (ABZ), as these coils provide pre-magnetization to the Z target liner. Using two capacitor banks (4 mF, 15 kV each) the system was designed to provide up to 900 kJ of energy[55]. Each set of coils are secured in the chamber in a test armature that replicates the Z shot hardware. Each set undergoes a series of test shots to verify its performance for the required Z shot parameters. The magnets can be pulsed with enough current to produce magnetic fields ranging from 10-30 T. For a 15 T shot, the peak current reaches about 12 kA.

3.3.1: MagLIF coils

Recent efforts to understand the mechanical effects from magnetic pressures led to installing a FIZ system in the ABZ chamber to record coil motion during a shot. Two FIZ configurations were utilized, one with a backlight (Figure 3.26) and another with frontal lighting (Figure 3.27). In the first configuration we attempted to video the change in gap spacing (or unexpected arcing) between the two coil leads. The camera used for this was a Chronos 1.4 CMOS camera, however data collection was not successful due to limited camera functionality. The second configuration positioned the lighting (specifically, four of the LED devices shown in Figure 3.26) at different angles in front of the coils to illuminate a tab extending from the support plate. An armature rod, concentric to the hole in the tab, was etched with rings (~400 μm width) with 1 mm spacing in between the rings (Figure 3.27a). This helped quantify the movement captured by the FIZ system. Like the Z shots, the imaging fiber was potted and passed through a vacuum flange. The wide-angle lens, described in Table 2.1, was used on the source side as shown in the photos that follow. It was secured to a small optical breadboard attached to the armature. Also, this vacuum chamber did not have installed lighting needed for video. Consequently, technicians worked to alter the battery-operated LED flashlights and built a switch box for external switching through a BNC feedthrough.

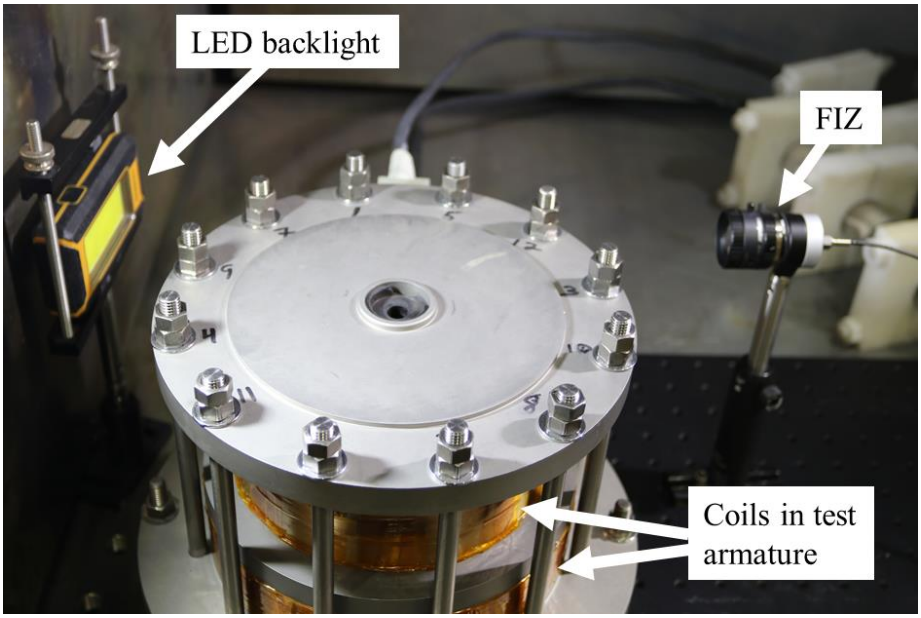

Figure 3.26 First FIZ configuration in ABZ vacuum chamber to observe coil movement via a backlit gap between leads.

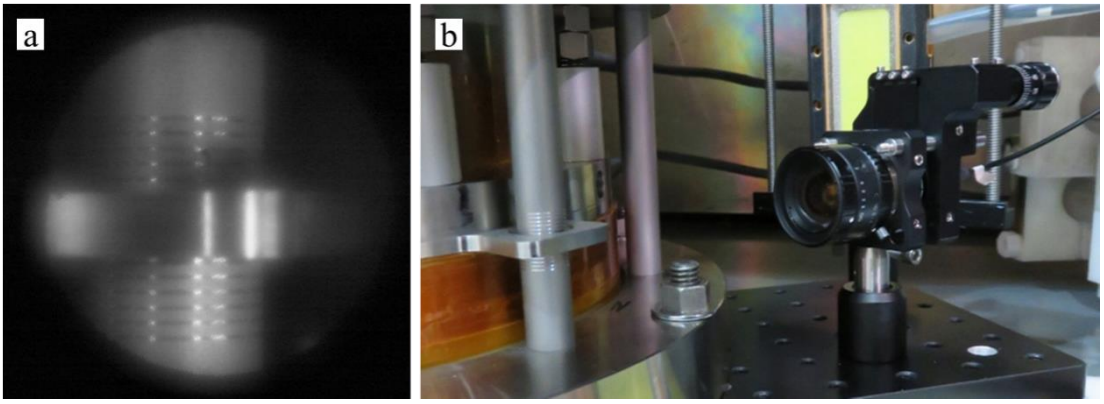

Figure 3.27 Second FIZ configuration in the ABZ vacuum chamber. System is focused on etched rod rings and an extended tab from the support plate between the coils. (a) Still from FIZ system video showing an approximate 2 cm FOV. (b) FIZ lens installed approximately 15 cm from the imaged support rod and tab.

While positioned in the second configuration, the Phantom® VEO multi-frame camera, described in section 2.2.2, was used to record the coil movement using 1 μs exposures at 10,000 frames per second. The first 60 frames of the video captured approximately 1 mm of upward movement for a 15 T shot. While further observation and analysis is needed to characterize this movement, the video captured was a meaningful first step to visualizing these effects.

The primary lessons from this application were as follows.

- For video, lighting is a challenge that can require significant planning and accommodation.
- In video of a pulsed power environment, it is tricky to isolate and analyze the movement of interest as contributions from the lens and lighting movement are also recorded.

CHAPTER 4: CONCLUSION

4.1: Summary

The purpose of this project was to develop and apply a new fiber imaging diagnostic for pulsed power experiments. The motivation was spurred by work on Sandia's Z machine, where low-density plasmas may reduce current to the load and impact MRT instabilities for MagLIF targets. Current imaging diagnostics are limited to a single line of sight and have resolution limitations or cumbersome installation requirements which further prompted this work.

The name of the new instrument is fiber imaging on Z (FIZ) and the key component of the system is a high-resolution plastic optical fiber (POF). The compact and versatile design utilizes lenses at either end of the POF to image and transmit self-emission onto a fast gated camera. Different focusing lens at the source side, and magnification at the sensor side, allows for a wide variety of imaging options.

Development and applications of the tool were discussed in this thesis providing details of the system's components and different installation designs. With different lens configurations (i.e., small diameter, wide-angle or objective) resolution results ranged from

3-700 microns with field of views ranging from 0.05-45 mm. FIZ was fielded on the Z and Mykonos accelerators, with varying results. Supplemental applications included laser shadowgraphy and video of mechanical motion.

4.2: Successes and Lessons Learned

Much was learned during the course of this project, and while success at Z remains outstanding, the achievements at Mykonos are encouraging. In particular, laser backlit shadowgraphy with the FIZ system will be fielded on upcoming Z shots due to the realization of this capability at Mykonos. As well, the successful bench testing with different lens configurations and controlled self-emission imaging opened the door for initial trials at Z which provided the following meaningful lessons.

While many lessons are shared throughout this thesis, the three that stand out as the most important are lighting, timing, and EMI screening. Foremost, it was found that lighting during installation (or operation) of the FIZ system is a real challenge due to reflective metal surfaces and concentrated light sources. Moving forward, a bright diffused light source (or several) would be ideal to optimize installation on future Z shots.

Second, determining when to trigger a fast gate camera during a nanosecond target implosion is incredibly difficult and requires a delay budget with a tiny bit of guess work. A lot of team effort went into measuring cable delays and calculating travel times, but more shot opportunities are needed to verify an optimal camera trigger time.

Last, is the issue of electromagnetic interference and unreliable data transfer. With the PI Max ICCD, everything is lost if the data does not make it to the laptop. This is a fundamental camera function that is now understood to need further EMI screening. For future Z shots, this camera will need to be in a screen room further away from the center section or will require more intensive shielding than previously provided. Again, this will require more testing to verify reliable performance.

4.3: Further Development

Many improvement and expansion ideas were proposed during the development of this instrument. As presented, some expansion ideas were implemented including debris

assessment on Z and coil movement in the ABZ chamber. At least two other areas are noted for future development, different fiber arrays and fiber coupling.

Construction of fiber arrays can be approached with different outcomes in mind. For example, one can maximize the camera sensor with an array on the sensor side of the system and have breakout fibers going to different locations on the source side. Figure 4.1 is a conceptual rendering of what a multi-view array could look like on the sensor side. Similarly, a breakout bundle could have fibers of different lengths to exploit inherent time delay. A first attempt to build a breakout fiber array is shown in Figure 4.2. Putting a fiber array on the source side if the system could increase field of view or create anti-parallel illumination and imaging by designated fibers as light sources.

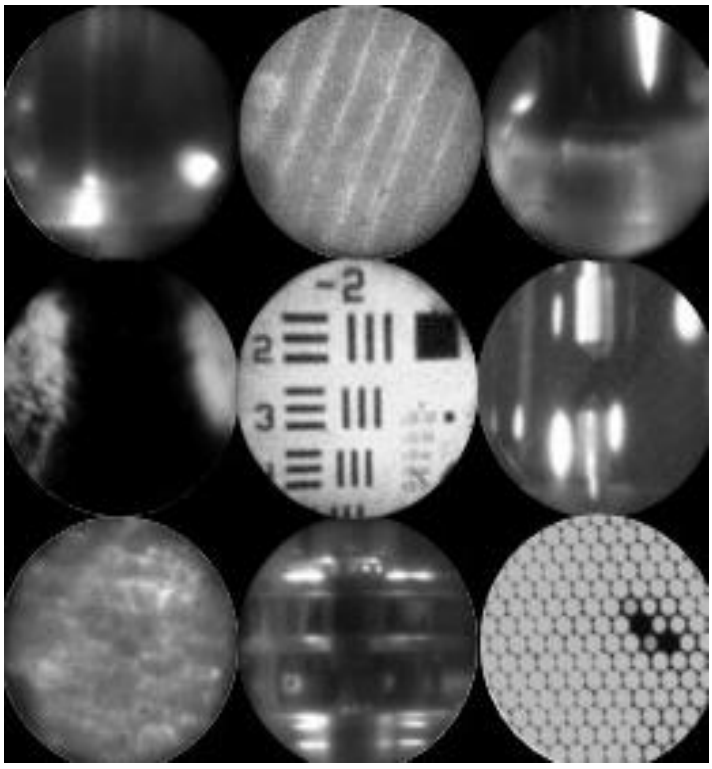

Figure 4.1 Conceptual rendering of multi-view configuration on one sensor.

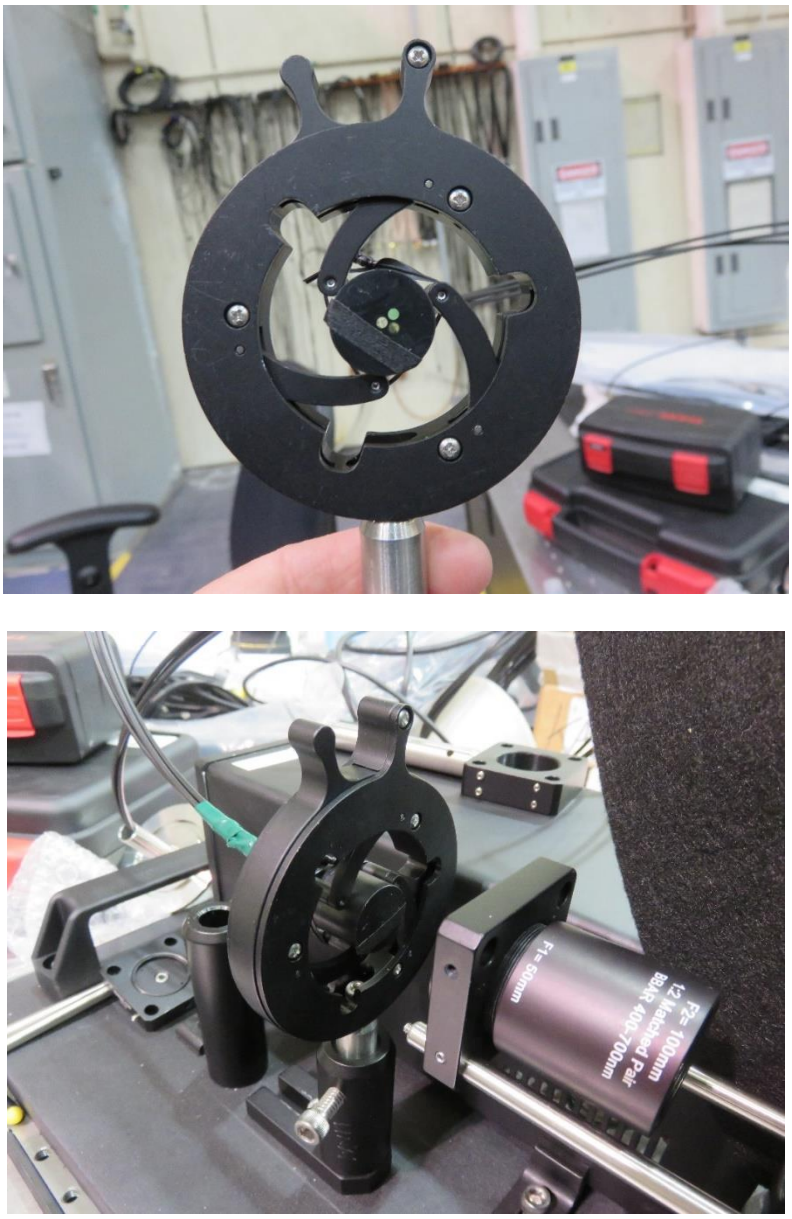

Figure 4.2 First attempt to build and image a breakout fiber array.

With regard to fiber coupling, two key issues can be addressed. 1) The fiber in the center section is destroyed but the fiber outside the center section remains intact and could be reused if fiber-to-fiber coupling was adequately employed. This is a strategy that is already being tested and is planned for future Z shots. 2) Lens-to-fiber coupling includes focused demagnification onto the 2 mm fiber face, but it also includes continued investigation of lens configurations to improve resolution and field of view.

REFERENCES

[1]D. A. Yager-Elorriaga *et al.*, *Nucl. Fusion* **62**, 042015 (2022).

[2]M. R. Gomez *et al., Phys. Rev. Lett.* **125**, 155002 (2020).

[3]N. Bennett *et al., Phys. Rev. Accel. Beams* **22**, 120401 (2019).

[4]N. Bennett *et al., Phys. Rev. Accel. Beams* **24**, 060401 (2021).

[5]D. B. Sinars, *et al., Phys. Plasmas* **27**, 070501 (2020).

[6]R. D. McBride *et al., Phys. Rev. Lett.* **109**, 135004 (2012).

[7]T. J. Awe *et al., Phys. Rev. Lett.* **111**, 235005 (2013).

[8]D. A. Yager-Elorriaga *et al.*, "Optical Imaging on Z LDRD: Design and Development of Self-Emission and Debris Imagers" (2021).

[9]A. S. Eddington, "45. The Internal Constitution of the Stars". *A Source Book in Astronomy and Astrophysics, 1900–1975*. Cambridge, MA and London, England: Harvard University Press, pp. 281-290 (2013).

[10]U.S Department of Energy (DOE/NE-0088), "The History of Nuclear Energy". Office of Nuclear Energy, Science and Technology, Washington, DC.

[11]I. D. Smith, "The Early History of Western Pulsed Power", *IEEE Transactions on Plasma Science*, vol. 34, no. 5, pp. 1585-1609 (2006).

[12]A. Van Arsdall and Sandia National Laboratories, "Pulsed power at Sandia National Laboratories: The first forty years". Albuquerque, N.M., Sandia National Laboratories (2007).

[13]R. B. Spielman *et al*., "PBFA II-Z: A 20-MA driver for Z-pinch experiments", *Digest of Technical Papers. 10th IEEE International Pulsed Power Conference* (1995).

[14]R. B. Spielman *et al*., *AIP Conference Proceedings* **195**, 3 (1989).

[15]D. H. McDaniel *et al*., "The ZR refurbishment project", *Conference Record of the Twenty-Fifth International Power Modulator Symposium, 2002 and 2002 High-Voltage Workshop* (2002).

[16]P. Rambo *et al., SPIE Proceedings* **10014** (2016).

[17]R. C. Kirkpatrick, Magnetized target fusion--An overview. United States: IEEE Service Center (1993).
[18]S. A. Slutz, *et al.*, *Phys. Plasmas* **17**, 056303 (2010).

[19]A. A. Kim, *et al.*, *Phys. Rev. ST Accel. Beams* **12**, 050402 (2009).

[20]D. V. Rose, *et al.*, *Phys. Rev. ST Accel. Beams* **13**, 090401 (2010).

[21]M. G. Mazarakis *et al.*, "Z driver post-hole convolute studies utilizing MYKONOS-V voltage adder," *19th IEEE Pulsed Power Conference* (2013).

[22]Asahi Kasei Corp., Model MCL-2000-24, High resolution plastic optical fiber, [Online]. Available: https://www.asahi-kasei.co.jp/ake-mate/pof/en/product/image-fiber.html. [Accessed March 2021].

[23]S. Abrate, R. Gaudino, and G. Perrone, "Step-Index PMMA Fibers and Their Applications", *Current Developments in Optical Fiber Technology*. IntechOpen, London (2013).

[24]P. Polishuk, *IEEE Communications Magazine* **44**, 9 (2006).

[25]S. Eve and J. Mohr, *Procedia Engineering* **1**, 1 (2009).

[26]A.D. Alobaidani *et al.*, *Optics and Lasers in Engineering* **48**, 5 (2010).

[27]Princeton Instruments, Model 4 1024f ICCD camera datasheet, [Online]. Available: www.princetoninstruments.com/wp-content/uploads/2020/04/PIMAX4_1024f_datasheet.pdf. [Accessed October 2020].

[28]Universeoptics, "Advantages of CCD Cameras", [Online]. Available: https://www.universeoptics.com/advantages-of-ccd-cameras/. [Accessed May 2022].

[29]Teledyne Princeton Instruments, "Fundamentals behind modern scientific cameras", [Online]. Available: https://www.princetoninstruments.com/learn/camera-fundamentals/fundamentals-behind-modern-scientific-cameras. [Accessed May 2022].

[30]Teledyne Princeton Instruments, "ICCD and emICCD Cameras: The Basics", [Online]. Available: https://www.princetoninstruments.com/learn/camera-fundamentals/iccd-and-emiccd-basics. [Accessed May 2022].

[31]Phantom®, "VEO 1310", [Online]. Available: https://www.phantomhighspeed.com/products/cameras/veo/veo1310. [Accessed September 2021].

[32]Edmund Optics, "Imaging Electronics 101: Understanding Camera Sensors for Machine Vision Applications", [Online]. Available: https://www.edmundoptics.com/knowledge-

center/application-notes/imaging/understanding-camera-sensors-for-machine-vision-applications. [Accessed June 2022].

[33]Thorlabs, Model R1DS1P positive 1951 USAF Test Target, Ø1", Available: https://www.thorlabs.com/thorproduct.cfm?partnumber=R1DS1P. [Accessed May 2022].

[34]Thorlabs, Model R3L3S1P positive 1951 USAF Test Target, 3" x 3", Available: https://www.thorlabs.com/thorproduct.cfm?partnumber=R3L3S1P. [Accessed May 2022].

[35]Oriel, Model 60000 Q series lamp housing, Available: https://www.newport.com/p/60000. [Accessed December 2020].

[36]Newport, Model 6427 Oriel Xenon flashlamps, Available: https://www.newport.com/medias/sys_master/images/images/hfb/hdf/8797196451870/Light-Sources.pdf. [Accessed December 2020].

[37]Oriel, Model 68826 Xe flashlamp power supply manual (2005).

[38]"1951 USAF resolution test chart", [Online]. Available: https://military-history.fandom.com/wiki/1951_USAF_resolution_test_chart. [Accessed January 2021].

[39]Teledyne Princeton Instruments, "LightField® Software", [Online]. Available: https://www.princetoninstruments.com/products/software-family/lightfield. [Accessed October 2020].

[40]Thorlabs, Model C220TMD-A mounted aspheric lens, [Online]. Available: https://www.thorlabs.com/thorproduct.cfm?partnumber=C220TMD-A. [Accessed January 2022].

[41]Computar, Model M0814-MP2 wide-angle lens, [Online]. Available: www.bhphotovideo.com/c/product/888985-REG/computar_M0814_MP2_2_3_Fixed_Lens.html. [Accessed July 2021].

[42]Swift, Model 20x 0.40 microscope objective lens, [Online]. Available: https://americanlaboratorytrading.com/lab-equipment-products/swift-20x-040-objective_16500. [Accessed May 2022].

[43]Thorlabs, Model MAP1050100-A matched achromatic doublet pair 1:2, [Online]. Available: www.thorlabs.com/thorproduct.cfm?partnumber=MAP1050100-A. [Accessed October 2020].

[44]Thorlabs, Model MAP1030100-A matched achromatic doublet pair 1:3.33, [Online]. Available: www.thorlabs.com/thorproduct.cfm?partnumber=MAP1030100-A. [Accessed October 2021].

[45]Teledyne Photometrics, “Saturation and Blooming”, [Online]. Available: https://www.photometrics.com/learn/imaging-topics/saturation-and-blooming. [Accessed November 2021]

[46]H. L. Anderson *et al.*, “Single Step Cutting and Polishing of Acrylic Optical Fibers Using a CO_2 Laser”, [Poster]. *41st PolyMAC Conference,* Albuquerque, NM (2012). Available: https://www.osti.gov/servlets/purl/1294508.

[47]M. E. Savage *et al*., "An overview of pulse compression and power flow in the upgraded Z pulsed power driver", *16th IEEE International Pulsed Power Conference* (2007).

[48]K. R. Lechien and J. M. Gahl, *IEEE Transactions on Plasma Science* **34**, 5 (2006).

[49]G. B. Frazier and S. R. Ashby, “Double-Bounce Switching”, *4th IEEE International Pulsed Power Conference* (1983).

[50]C. Ball and J. Lash, “Capability Advances at the Sandia Z Machine”, [Power Point] (2015).

[51]C. E. Myers *et al*., *Review of Scientific Instruments* **92**, 033501 (2021).

[52]T. A. Shelkovenko *et al., IEEE Transactions on Plasma Science* **42**, 3 (2014).

[53]T. A. Shelkovenko *et al., Plasma Phys. Rep.* **41** (2015).

[54]Edmund Optics, 40 mm Dia. x 400 mm FL, Available: www.edmundoptics.com/p/400mm-dia-x-4000mm-fl-uncoated-plano-convex-lens/5770/. [Accessed April 2022]

[55]D. C. Lamppa *et al.*, “Electromagnet Designs on Low-Inductance Power Flow Platforms for the Magnetized Liner Inertial Fusion (MagLIF) Concept at Sandia's Z Facility”, [Power Point]. *IEEE International Power Modulator and High Voltage Conference* (2018).